Diplomarbeit

Enabling real-time feedback for LTE measurements with the Vienna MIMO Testbed

ausgeführt zum Zwecke der Erlangung des
akademischen Grades eines Diplom-Ingenieurs

unter der Leitung von
Univ. Prof. Dipl.-Ing. Dr.techn. Markus Rupp
Dipl.-Ing. Martin Lerch
Institute of Telecommunications

eingereicht an der Technischen Universität Wien
Fakultät für Elektrotechnik und Informationstechnik

von
Michael Meidlinger Bsc

Matr. Nr.: 0728169
Weingartenweg 35/1/2
A-7123 Mönchhof

Wien, im November 2013

Abstract

The ever increasing demand for higher mobile data rates continues to rise challenges for researchers and developers. As the the available spectral resources remain essentially the same, the key to higher data rates lies in improving spectral efficiency. Multiantenna techniques are one of the most important technologies to enhance spectral efficiency, enabling the transmission of multiple spatially separated data streams as well as increasing the receive signal quality, which in turn allows for higher data rates.

Predecessor technologies such as WiMAX[1] and HSDPA[2] begun to support multi-antenna techniques as well as adaptive modulation and coding. Following this trend, recent standards such as LTE[3] and LTE-A[4] continue to support more antennas and modulation and coding schemes. Hence, whereas a brute force approach of transmitting and evaluating all possible signals was feasible for those legacy systems, the amount of differently modulated, coded and spatially preprocessed signals exceeds practical limits in the case of LTE and LTE-A.

In order to still characterize the throughput performance of LTE and LTE-A MIMO[5] systems by means of measurements, the channel state needs to be evaluated and fed back in a real-time fashion. Based on this feedback, the transmitter can determine the appropriate parameters and transmit only the signal that best matches the current channel state.

Throughout this thesis, the Vienna MIMO Testbed, which has been used to measure various mobile communication standards in the past, is augmented by a feedback mechanism for LTE and LTE-A. The thesis specifies the key requirements for such a system and describes the implementation in form of a software extension. Finally, measurement results indicating the consistency and validity of the proposed system are presented. More over, the results provide novel measurement-based performance figures for LTE-A systems.

[1] Worldwide Interoperability for Microwave Access
[2] High Speed Downlink Packet Access
[3] Long Term Evolution
[4] LTE-Advanced
[5] Multiple Input- Multiple Output

Kurzfassung

Der stetig steigende Bedarf an mobilem Datenverkehr stellt Entwickler und Forscher immer wieder vor neue Herausforderungen. Da das verfügbare Frequenzspektrum im Wesentlichen gleich bleibt, liegt der Schlüssel zu höheren Datenraten von Basisstation zu Endgerät in einer Steigerung der spektralen Effizienz. Multiantennensysteme gelten als eine der wichtigsten Technolgien zur Verbesserung der spektralen Effizienz. So können unter Zuhilfenahme multipler Sende- und Empfangsantennen mehrere räumlich getrennte Datenströme übertragen werden, bzw. lässt sich so die Signalqualität am Empfänger steigern, was wiederum höhere Datenraten erlaubt.

Während zwar auch Vorgängertechnologien wie WiMAX[1] und HSDPA[2] MIMO[3] Techniken sowie adaptive Modulation und Codierung unterstützen, so geht der Trend für die aktuellen Standards LTE[4] und LTE-A[5] in die Richtung von immer mehr Antennen und immer genauere Anpassung des Sendesignals an den Kanalzustand. Aus diesem und anderen Gründen können wegen der schieren Anzahl an möglichen Parameterkonfigurationen nicht mehr alle möglichen Sendesignale übertragen und ausgewertet werden.

Um trotzdem eine messtechnische Erfassung des Datendurchsatzes von LTE und LTE-A zu ermöglichen, bedarf es daher einer Echtzeit-Auswertung und Rückführung des Kanalzustandes vom Empfänger zum Sender. Auf Basis dieser Information kann dann im Sender das kanalangepasste Sendesignal erzeugt und übertragen werden.

Im Zuge dieser Arbeit wurde das Vienna MIMO Testbed, welches auch bisher bereits für die Messung von Mobilfunksystemen mit mehreren Antennen verwendet wurde, um einen solchen Rückführungsmechanismus für LTE und LTE-A Signale erweitert. Die vorliegende Arbeit beschreibt die wesentlichen Aufgaben die so ein System zu erfüllen hat, sowie dessen Implementation in Form einer Software-Erweiterung. Zum Ende werden Messergebnisse präsentiert, welche die Konsistenz des entworfenen Systems zeigen und die gewählte Vorgehensweise rechtfertigen. Darüber hinaus stellen die präsentierten Messergebnisse auch neue Resultate über die Leistungsfähigkeit eines LTE-A Systems dar.

[1] Worldwide Interoperability for Microwave Access
[2] High Speed Downlink Packet Access
[3] Multiple Input- Multiple Output
[4] Long Term Evolution
[5] LTE-Advanced

Acknowledgement

First of all, I would like to thank my supervisor Prof. Markus Rupp for introducing me to academic research and giving me the opportunity to collect valuable experience in the field of mobile communication research.

Many thanks go to my second supervisor Martin Lerch for making me realize that there is a whole bunch of hardware related aspects I never considered before working on this thesis, as well as for his support throughout the thesis.

I would also like to thank my colleagues at the Institute of Telecommunications, especially Stefan Schwarz for helping me understand the feedback related aspects of this work, my colleague and good friend Martin Müller for his motivation and support and Ronald Nissel for fruitful discussions.

But my biggest thanks go to my parents Gerlinde and Josef, for their continuous encouragement and for teaching me the most important things in life.

Contents

1 Motivation **1**

2 The LTE physical and MAC layer **5**

2.1 The physical resources 5

2.2 MIMO 7

2.3 LTE physical and MAC layer processing 9

2.4 MIMO transmission modes in LTE-(A) 10

2.4.1 SU-MIMO Modes 11

2.4.2 MU-MIMO Modes 13

3 The Vienna MIMO Testbed **16**

3.1 Hardware 16

3.1.1 Transmitter Hardware 17

3.1.2 Receiver Hardware 19

3.2 Software 19

3.2.1 Daemon Software 19

3.2.2 Matlab Software 21

4 Measuring with real-time feedback **22**

4.1 Feedback definition and calculation 23

4.2 The measurement procedure 24

4.2.1 The feedback link 25

4.2.2 Downconversion and Upconversion 25

4.2.3 SNR- and channel estimation 26

4.2.4 Coding and symbol mapping 29

4.3 Software Overview 29

4.3.1 Measurement script 30

4.3.2 Simulation script 31

4.3.3 Evaluation script 31

5 Measurement based evaluation **32**

5.1 Impact of the delay 32

5.2 Measurement vs. Simulation 35

6 Conclusion and Outlook **38**

Bibliography **40**

A Acronymes **43**

Chapter 1

Motivation

In the recent past the mobile communication standard Long Term Evolution (LTE) has been designed to fill the ever increasing need for higher mobile data rates under the constraint of limited spectral resources. Whereas the rollout of LTE has already commenced all over the world and devices supporting LTE can yet be found on the market, its predecessor[1] LTE-A is still in the specification and testing phase. There is currently a lot of research on LTE-A compliant algorithms and candidate technologies for future LTE releases —mostly evaluated by means of numerical Monte Carlos simulations— but little is known about the performance and feasibility of this algorithms when transmission is not simulated but rather carried out over a real radio channel.

In [23], the Multiple Input- Multiple Output (MIMO) Testbed described in [10, 15] is used for transmitting LTE signals generated with the LTE Link-Level Simulator [26] over a real radio channel. Signals are generated offline for any possible set of transmission parameters and saved to files which are then transmitted via the Testbed. At the receiver, the signals are written to disk for subsequent offline evaluation by a cluster of PCs. In the evaluation process, all the signals are analyzed and the one performing best —corresponding to the best choice of transmission parameters— is selected. Using this brute force approach, the best choice of parameters, which depends on time varying channel conditions, can be determined offline without the need for real-time feedback.

However, one can not simply reuse the brute force approach for LTE-A measurements by substituting the LTE Link-Level Simulator with an LTE-A Simulator (e.g. [22]). To elaborate this statement, we have to take a look at the differences regarding spatial multiplexing between LTE and LTE-A.

LTE-A supports MIMO transmission with up to 8 transmit antennas. This allows for the use of enhanced spatial multiplexing schemes that can transmit up to 8 data streams in parallel on one and the same time-frequency resource. As most User Equipments (UEs) are constrained in size and battery due to their mobile nature and therefore can

[1] More precisely, LTE-Advanced (LTE-A) is part of the *evolution* LTE was designed to undergo during its life cycle as a mobile communication standard. LTE is specified in 3GPP Rel. 8 and LTE-A in 3GPP Rel. 10. Future releases are expected to continue the evolution in improving the system performance.

only implement a limited number of receive antennas and Radio Frequency (RF) chains, Multi User MIMO (MU-MIMO) transmission is needed to fully exploit the potential of all the transmit antennas. MU-MIMO is a technique where multiple UEs are served on the same time-frequency resource and are only separated in the spatial domain. Usually this separation is achieved by appropriate precoding, which effectively steers multiple non interfering beams to the individual UEs. Therefore, LTE-A supports non-codebook based precoding, enabling the cancellation of interference between streams intended for different UEs at the base station site. As a consequence, an LTE-A base station —also referred to as eNodeB— is capable of utilizing its full transmission capacity even if there are only UEs with one or two receive antennas, which is a fairly common scenario.

So from a theoretical perspective, the continuum of possible precoders permits the brute force approach being utilized in [23]. However, this approach is also limited by practical considerations: It is computationally expensive so that a measurement of, e.g., 4×4 LTE closed loop mode could not yet be performed, as the number of possible parameter combinations is prohibitive and —as the evolution of LTE continues— ever increasing.

To overcome this limitations and measure the performance of higher order MIMO LTE and LTE-A, an integrated approach is required where the channel state is evaluated online and fed back to the transmitter in a real-time fashion. This thesis presents such an approach and its implementation in form of a software extension to the Vienna MIMO Testbed. The software integrates functionality from the Vienna LTE-A Link Level Simulator with the Vienna MIMO Testbed, thereby extending the capabilities of the testbed in the following ways:

Measurement of enhanced MIMO schemes As stated above, the support of non codebook based precoding enables a variety of MU-MIMO transmission schemes such as Zero Forcing (ZF) MU-MIMO [28] and block diagonalization [32]. For these schemes, real-time feedback is vital and can not be substituted by exhaustive transmissions.

Frequency selective scheduling The measurements based on the brute force approach focus on the single user scenario where one eNodeB communicates with one UE. In this scenario, due to standard constraints, the same Modulation and Coding Scheme (MCS) is used for the entire system bandwidth. In real systems however, the frequency selectivity of the channel is respected by adopting the MCS to the channel conditions in the respective frequency sub-band. For a thorough treatment of this aspect, the reader is referred to [27].

Hybrid Automatic Repeat reQuest (HARQ) On the Medium Access Control (MAC) layer, LTE relies on HARQ for error correction and detection. With the use of real-time feedback, the impact of HARQ on the system performance can be investigated (cf. [27]).

Reduction in computational effort Using the brute force approach, the evaluation of all signals can take weeks even when delegated to a cluster of PCs. Assuming 4×4 LTE open loop transmission with any combination 15 possible MCSs, 4 possible transmission ranks, 30 levels of transmit power and 100 realizations, $(15 + 3 \cdot 15^2) \cdot 30 \cdot 100 = 2\,070\,000$ subframes have to be transmitted and evaluated[2]. If we further assume a mean evaluation time of 2.5 seconds/subframe [15], the evaluation of this measurement takes about 2 months on a single PC. Now we can see why a measurement of 4×4 LTE closed loop has not been possible so far: Another 16 possibilities for the choice of the precoder is simply not feasible anymore. Moreover, the possibility for 8×8 transmissions in LTE-A requires a new approach. By using real-time feedback, the evaluation time can be reduced dramatically so that a performance evaluation of higher order MIMO modes becomes possible.

Despite all these enhancements, an approach based on real-time feedback comes at a price: First of all, there is an inevitable delay between the time when the feedback is calculated at the receiver and a new signal incorporating the feedback is generated and sent at the transmitter. Secondly, any feedback algorithm is suboptimal[3], so that the maximum system capacity is in general not achieved, whereas this was guaranteed by the brute force approach. If, however, appropriate measures are taken, the delay can be minimized to an extend where the out dating of the Channel State Information (CSI) is negligible (cf. Chapter 4 and Section 5.1).

One of the main design goals for the software presented in this thesis was thus to minimize the delay. To address the issue of suboptimal feedback, the measurement part of the software is accompanied by a simulative part, which allows for comparisons against the optimal case.

The rest of this work is structured as follows:

Chapter 2 introduces the LTE physical and MAC layer. The physical resources and system model of a MIMO Orthogonal Frequency-Division Multiplexing (OFDM) system are presented, followed by a description of different LTE/LTE-A MIMO transmission modes along with the respective feedback information.

Chapter 3 presents the measurement hardware and software, giving insight into hardware related constraints and explains how the MATLAB software integrates into the Vienna MIMO Testbed.

Chapter 4 builds on the findings of Chapters 2 and 3 and introduces the feedback functions employed. Subsequently, this chapter specifies the tasks that the mea-

[2]For rank 1, there are 15 possibilities for the MCS, whereas for higher ranks, two independent MCSs are supported.

[3]Any real system involves noise, i.e., a random disturbance of the signal. While the average amount of noise can be taken into account by a feedback function, the exact noise realization is never known prior to transmission. More over, practical feedback functions target a block error rate around 0.1 in order not to be too conservative in the choice of the MCS. The residual errors are compensated through HARQ retransmissions.

surement software has to perform and discusses how a fast implementation can be achieved.

Chapter 5 presents and interprets measurement and simulation results, verifying the consistency of the measurement approach.

Chapter 6 concludes this work with a summary and an outlook on possible measurements and improvements.

Chapter 2

The LTE physical and MAC layer

2.1 The physical resources

Similarly to other high performance wireless communication technologies such as WiMAX or the Wifi standards IEEE 802.11a/g/n, LTE relies on OFDM as a modulation and multiplexing scheme.

In general, an OFDM modulator maps the transmit symbols $x_{n,k}$ to the transmit signal $s(t)$ according to

$$s(t) = \sum_{n=-\infty}^{\infty} s_n(t) = \sum_{n=-\infty}^{\infty} \sum_{k=0}^{K-1} x_{n,k} g(t - nT) \mathrm{e}^{\mathrm{j}2\pi kFt} \,, \tag{2.1}$$

where n is the temporal OFDM symbol index, $k \in \{0, 1, \ldots, K-1\}$ is the subcarrier index, F is the subcarrier spacing and $g(t)$ is the transmit pulse shape. If we choose a rectangular pulse

$$g(t) = \begin{cases} \sqrt{F}, & 0 \leq t < T \\ 0, & \text{otherwise} \end{cases} \,, \tag{2.2}$$

with pulse duration $T = 1/F$ and sample the signal at the time instants

$$mT_s = mT/K \,, \qquad m \in \mathbb{Z} \,, \tag{2.3}$$

the sampled version of the n-th OFDM symbol is given by

$$s_n[m] = \frac{1}{\sqrt{K}} \sum_{k=0}^{K-1} x_{n,k} \mathrm{e}^{\frac{\mathrm{j}2\pi km}{K}} = \mathrm{IDFT}_{k \to m}\{x_{n,k}\} \,. \tag{2.4}$$

Inversely, the corresponding OFDM demodulator attempts to extract the transmit symbols $x_{n,k}$ from the receive signal $r_n[m]$ by means of a Discrete Fourier Transform (DFT):

$$y_{n,k} = \mathrm{DFT}_{m \to k}\{r_n[m]\}. \tag{2.5}$$

Assuming a linear, time-invariant[1] channel with impulse response $h[l]$ and additive, white Gaussian noise $z[m] \sim \mathcal{CN}(0, \sigma_z^2)$, the receive signal $r[m]$ is given by

$$r[m] = (h * s)[m] + z[m] \tag{2.6}$$

If we further extend the transmit OFDM symbols $s_n[m]$ by a cyclic prefix of length N_{CP} and ensure that $h[l] = 0$ for $l \geq N_{\mathrm{CP}}$, the convolution in Equation (2.6) amounts to a cyclic convolution. Combining this result with Equation (2.4) and Equation (2.5), we arrive at the well known OFDM input-output relation in the frequency domain:

$$y_{n,k} = H_k x_{n,k} + z_{n,k} \ , \tag{2.7}$$

with $H_k = \mathrm{DFT}_{l \to k}\{h[l]\}$ and $z_{n,k} \sim \mathcal{CN}(0, \sigma_z^2)$. Assuming a normalized model with $\mathrm{E}\{H_k\} = \mathrm{E}\{x_{n,k}\} = 1$ as well as mutually uncorrelated channel, transmit symbols and noise, the Signal to Noise Ratio (SNR) is given by $\mathrm{SNR} = 1/(\sigma_z)^2$. As we will see in the subsequent sections, Equation (2.7) is the fundamental relation on which most of the frequency domain signal processing for OFDM signals builds upon.

In LTE terminology, the resource indexed by the time n and subcarrier k is called a Resource Element (RE): It is the fundamental physical resource and can carry exactly one modulation symbol $x_{n,k}$ from a predefined symbol alphabet, e.g., 4-QAM, 16-QAM or 64-QAM.

The subcarrier spacing F is specified to be 15 kHz in the LTE standard, whereas the number of subcarriers K depends on the system bandwidth. Table 2.1 gives an overview of the available resources for different LTE system bandwidths.

System bandwidth [MHz]	1.4	3	5	10	15	20
Number of Resource Blocks (RBs) N_{RB}	6	15	25	50	75	100
Number of data subcarriers $K = N_{\mathrm{RB}} N_{\mathrm{sc}}^{\mathrm{RB}}$	72	180	300	600	900	1200
Transmission bandwidth $B = KF$ [MHz]	1.08	2.7	4.5	9	13.5	18
Guardband size	23%	10%	10%	10%	10%	10%

Table 2.1: Resources for different LTE system bandwidths [1]

In order to keep the signalling overhead small whilst still allowing for frequency and time selective precoding and MCSs, LTE groups several REs together to one RB, which is the fundamental resource for the MAC layer. Consequently, scheduling assignments are always granted in multiples of RBs and also the feedback is provided in resource block granularity.

If MIMO is employed along with OFDM, the LTE physical resources, in addition to time and frequency, also span over the spatial domain. Hence, for that case, a RE is indexed by the triple (n, k, ν), where ν is the spatial index, cf. Section 2.2.

[1] In general, a linear mobile radio channel is characterized by a time variant impulse response $h[l, m]$. Since we are considering static scenarios, the channel change during the duration of one OFDM symbol is negligible.

Figure 2.1 visualizes the 3-dimensional physical LTE resource grid.

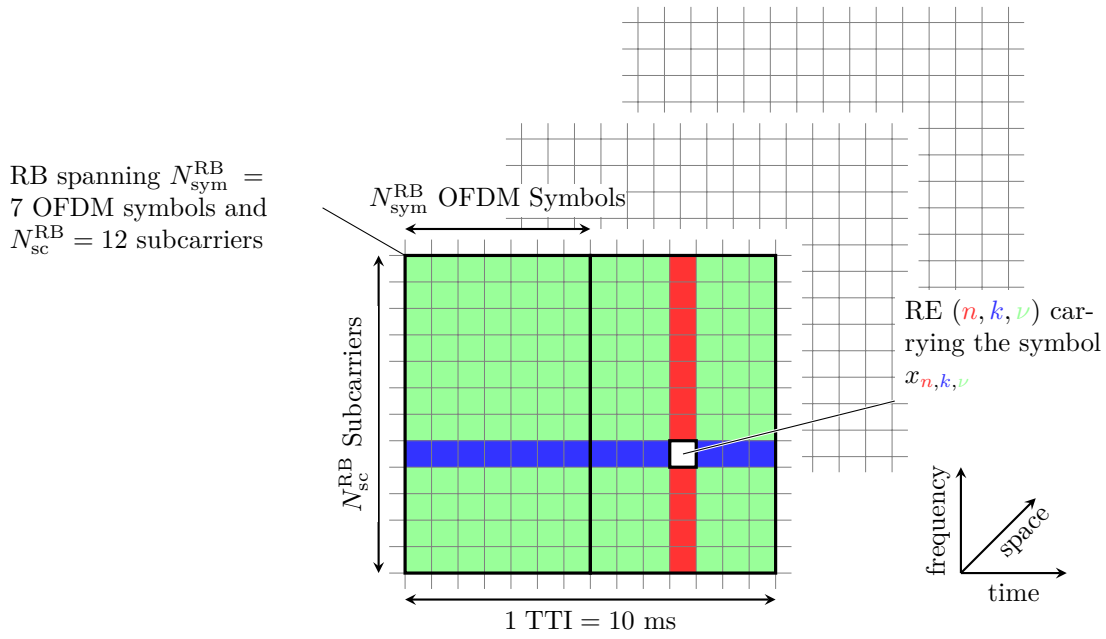

Figure 2.1: The physical resource in LTE.

2.2 MIMO

Now let us consider MIMO transmission with N_{TX} transmit antennas and N_{RX} receive antennas with $s_j(t)$ being the transmit signal[2] on antenna j, $r_i(t)$ being the signal received at antenna i and $h_{i,j}(t)$ being the channel impulse response between those antennas, cf. Figure 2.2. Taking into account the linearity of the radio channel and focusing on the sampled signals, Equation (2.6) can be generalized to

$$r_i[m] = \sum_{j=1}^{N_{\text{TX}}} (h_{i,j} * s_j)[m] + z_i[m] \; . \tag{2.8}$$

Combining Equation (2.5) with Equation (2.8) we obtain the generalized version of Equation (2.7)

$$y_{n,k,i} = \sum_{j=1}^{N_{\text{TX}}} H_{k,i,j} x_{n,k,j} + z_{n,k,i} \; , \tag{2.9}$$

which, when considering all the receive signals, can be written in a more compact matrix vector notation:

$$\mathbf{y}_{n,k} = \mathbf{H}_k \mathbf{x}_{n,k} + \mathbf{z}_{n,k} \, . \tag{2.10}$$

[2]Please note that, in contrast to Equation (2.1) the index j refers to the transmit antenna rather then to the OFDM symbol.

Since we assume spatially uncorrelated noise with equal variance on all antennas, the channel is perfectly characterized by the knowledge of the pair $(\mathbf{H}_k, \sigma_z^2)$, which we will refer to as *perfect* CSI.

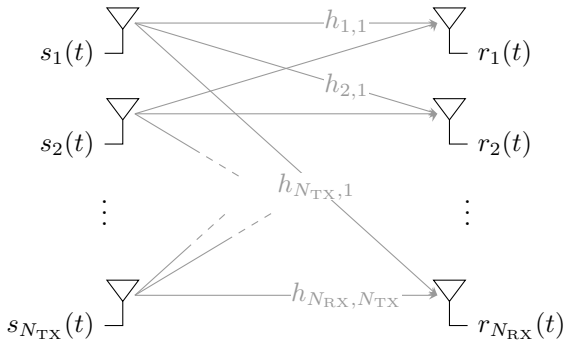

Figure 2.2: MIMO

In order to allow for linear spatial preprocessing, Equation (2.10) can be adopted as follows:

$$\mathbf{y}_{n,k} = \mathbf{H}_k \mathbf{x}_{n,k} + \mathbf{z}_{n,k} = \mathbf{H}_k \underbrace{\mathbf{P}_{n,k} \mathbf{x'}_{n,k}}_{\mathbf{x}_{n,k}} + \mathbf{z}_{n,k} \,. \tag{2.11}$$

Thus, instead of directly transmitting the N_{TX} symbols $\mathbf{x}_{n,k}$, we apply a linear precoding matrix $\mathbf{P}_{n,k} \in \mathbb{C}^{N_{\mathrm{TX}} \times L}$ to the L symbols $\mathbf{x'}_{n,k}$ and transmit the product of symbols and precoder. As we will see in more detail in Section 2.4, precoding can serve various purposes. For now, it is sufficient to note that by employing a precoder, we gain another degree of freedom, as the *effective channel* $\mathbf{A}_{n,k} = \mathbf{H}_k \mathbf{P}_{n,k}$ mapping the L symbols $\mathbf{x'}_{n,k}$ to the N_{RX} symbols $\mathbf{y}_{n,k}$ can be influenced by the precoder. In this context, L is called the number of layers, i.e., the number of spatial streams transmitted in parallel. In the following, the symbol- and subcarrier index (n, k) will be dropped if possible.

Until now, we did not specify whether the receive signals $r_i(t)$ in Figure 2.2 are intended for one UE with N_{RX} receive antennas or for multiple UEs with N_{RX} receive antennas in total. The former scenario is called Single User MIMO (SU-MIMO) while the latter is referred to as MU-MIMO. Where as the physical situation is the same, MU-MIMO and SU-MIMO differ in the channel knowledge that can be obtained at the transmitter: While the SU-MIMO terminal can estimate the full channel $\mathbf{H}$, a UE operating in MU-MIMO mode can only know its $N_{\mathrm{RX},u} \times N_{\mathrm{TX}}$ channel matrix $\mathbf{H}_u$, where

$$\mathbf{H} = \begin{bmatrix} \mathbf{H}_1 \\ \mathbf{H}_2 \\ \vdots \\ \mathbf{H}_{N_{\mathrm{UE}}} \end{bmatrix}, \qquad \sum_{u=1}^{N_{\mathrm{UE}}} N_{\mathrm{RX},u} = N_{\mathrm{RX}} \,. \tag{2.12}$$

As a result, the feedback strategies for SU-MIMO and MU-MIMO are quite different, as will be shown in Section 2.4.

2.3 LTE physical and MAC layer processing

In order to incorporate feedback into measurements with the Vienna MIMO Testbed, one also has to consider the MAC layer for signal generation. Figure 2.3 gives an overview of the transmitter side signal processing for generating a MIMO OFDM signal.

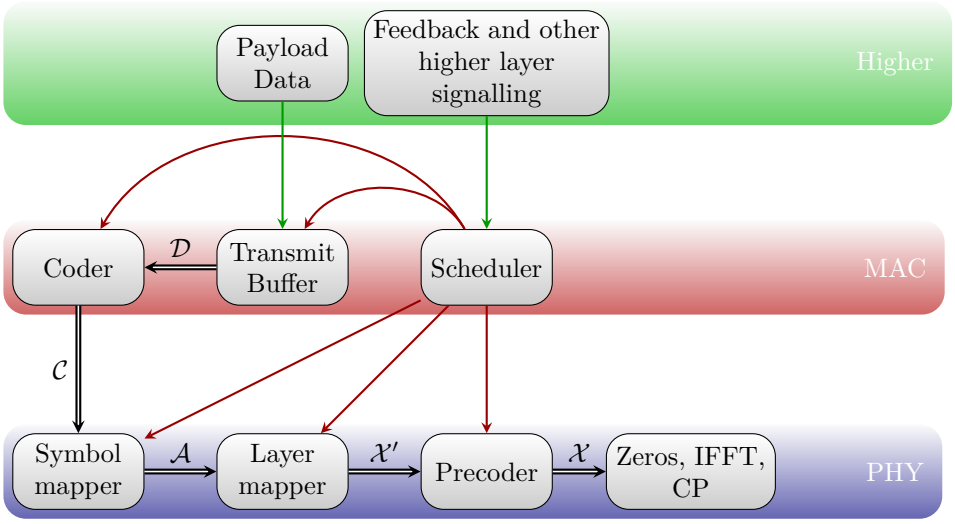

Figure 2.3: Physical and MAC layer processing in LTE. The data flow is represented by the black arrows. The red arrows represent the influence of the scheduler on the parameters of the respective functional block (e.g. choice of MCS for the coder and the symbol mapper, etc.). Control information and payload data from higer layers is symbolized by the green arrows.

Scheduler The scheduler can be viewed as the implementation of the LTE MAC layer. It receives UE feedback originating from measurements at the PHY layer as well as other control information such as type of service information, which enables it to, e.g., prioritize realtime data such as Voice over IP. Every Time-Transmission Interval (TTI), the scheduler determines how many spatial layers L are used and (in the closed loop case) how they are going to be precoded, as well as what users transmit on which RBs with what MCS. Please note that, in the most general case, all these decisions are taken in a RB granularity, thus making them time and frequency dependent.

In addition, the scheduler also keeps track of the HARQ process. The important role of the scheduler is treated in more detail in [27].

Transmit buffer According to the scheduling decision, a set of P datawords $\{\mathbf{d}_1, \ldots, \mathbf{d}_P\} = \mathcal{D}$ of various lengths L_p, $p = 1, \ldots, P$ is selected for transmission. Because of standard constraints, there can be at most two datawords per UE during one TTI.

Coder The coder individually maps the P datawords $\mathbf{d}_p$ to the set of P codewords $\mathcal{C}$ according to the code rate implied by the MCS scheduling decision.

Symbol Mapper The symbol mapper maps the P codewords to the set of P symbol

vectors $\mathcal{A} = \{\mathbf{a}_1, \ldots, \mathbf{a}_I\}$ according to the modulation alphabet implied by the MCS scheduling decision.

Layer mapper The layer mapper fills the 3-dimensional resource grid shown in Figure 2.1 with the symbol vectors $\mathcal{A}$ according to the scheduling decision. We can formally describe the grid for one TTI by the set of vectors $\{\mathbf{x'}_{n,k}\}$ with $n = 1, \ldots, 2N_{\text{sym}}^{\text{RB}}$ and $k = 1, \ldots, K$. As the number of spatial layers L can in general vary from RB to RB, we can formally write $L = L_{n,k}$ to denote its time and frequency dependence.

Precoder The precoder maps the symbols $\mathbf{x'}_{n,k}$ from the layer domain to the transmit antenna domain by computing the set of transmit symbols

$$\mathcal{X} = \{\mathbf{x}_{n,k}\} = \{\mathbf{P}_{n,k}\mathbf{x'}_{n,k}\} \,, \tag{2.13}$$

where $\mathbf{P}_{n,k} \in \mathbb{C}^{N_{\text{TX}} \times L_{n,k}}$ is the linear precoding matrix for RE (n, k) and N_{TX} denotes the number of transmit antennas.

Zeros, IFFT, CP This block maps the set of transmit symbols $\mathcal{X}$ to the time domain by computing the Inverse Discrete Fourier Transform (IDFT), cf. Equation (2.4). For reasons of computational efficiency, the K-point IDFT is replaced by an Inverse Fast Fourier Transform (IFFT) of length

$$K_{\text{FFT}} = 2^{\lceil \log_2 K \rceil} \geq K \tag{2.14}$$

and $x_{n,k}$ is augmented with zeros for $K \leq k \leq K_{\text{FFT}}$, yielding the same OFDM symbol $s_n[m]$. Eventually, $s_n[m]$ is prepended by its Cyclic Prefix (CP) to avoid inter symbol interference.

2.4 MIMO transmission modes in LTE-(A)

LTE defines several MIMO transmission modes to optimally employ all the available transmit and receive antennas. The more sophisticated a modes' multi antenna technique is, the more feedback information is necessary at the transmitter. At the same time, more accurate feedback implies a channel that is constant over a longer period of time, given that the feedback intervals are constant[3]. Ideally, perfect CSI $(\mathbf{H}_k, \sigma_z^2)$ at the transmitter is desirable but would of course cause too much overhead on the uplink channel[4]. Consequently, LTE defines several feedback parameters that contain condensed, implicit CSI applicable to the respective MIMO transmit mode.

[3]The average rank of the channel matrix $\mathbf{H}$ is determined by the scattering environment, where as the individual elements of the matrix are determined by the small scale fading environment, which varies considerably faster then the macro scale scattering

[4]In this work, we only consider the Frequency Division Duplexing (FDD) mode of LTE, where the channel can only be estimated at the receiver.

LTE Release 8 [2] defines 7 different MIMO transmission modes for up to four transmit antenna ports[5]. So called Cell specific Reference Symbols (C-RS) are used to estimate the channel $\mathbf{H}$ for both demodulation and feedback calculation. For demodulation, the precoder as chosen by the eNodeB has to be signaled to the UE via a control channel, thus limiting the spatial preprocessing to linear codebook based precoding.

In order to reach the targets for 4G communication [19], improve the cell edge capacity and to overcome some limitations of the LTE modes, the LTE-A Release 10 [3, 4] specifies downlink transmission on up to 8 antenna ports along with a new Reference Symbol structure, employing different RS for demodulation and CSI feedback. Precoded User specific Reference Symbols (UE-RS) are used for estimating the effective channel $\mathbf{A} = \mathbf{HP}$ for demodulation, allowing the eNodeB to use non codebook based precoding, while the physical channel $\mathbf{H}$ is estimated via CSI Reference Symbols (CSI-RS) and is used for deriving CSI feedback [24, 29].

Table 2.2 gives an overview of all the modes specified up to Release 10; more detailed information on the most relevant modes can be found in the subsequent section.

Mode	Description	L	Release	RS	Application Scenario		
					SNR	Scattering	Speed
1	Single Antenna	1	8	C-RS	–	–	–
2	Transmit Diversity	1	8	C-RS	Low	Low	High
3	OLSM	2-4	8	C-RS	High	High	High
4	CLSM	2-4	8	C-RS	High	High	Low
5	LTE MU-MIMO	2-4	8	C-RS	High	–	Low
6	Single layer CLSM	1	8	C-RS	Low	Low	Low
7	Single layer beamforming	1	8	C-RS/UE-RS	Low	Low	Low
8	Dual layer beamforming	1-2	9	C-RS/UE-RS	Low	–	Low
9	Dynamic SU- and MU-MIMO	1-8	10	CSI-RS/UE-RS	–	–	Low

Table 2.2: LTE and LTE-A MIMO transmission modes and their application scenarios [33]

2.4.1 SU-MIMO Modes

For SU-MIMO, the full channel $\mathbf{H}$ from Equation (2.12) is known at the receiver. Consequently, the interference between the spatial layers can be estimated at the UE, allowing it to autonomously choose transmission rank, precoder and MCS. These parameters are fed back to the eNodeB, providing it with implicit CSI.

[5] In the LTE standards, an antenna port is defined by its Reference Symbol (RS) structure. Release 8, for example, defines 4 antenna ports where C-RS are transmitted, allowing the UE to resolve up to 4 streams. However, the number of physical antennas is not restricted, as N_{ports} antenna ports can be mapped to $N_{\text{TX}} \geq N_{\text{ports}}$ via a semi static precoder that is transparent to the UEs, providing additional transmit diversity.

Mode 1 and 2

Unlike the other modes described in this section, mode 1 and mode 2 only transmit one spatial stream and are therefore not considered in detail in this work.

Mode 1 supports only one transmit antenna and hence does not involve any spatial preprocessing at the tranmitter. However, Single Input - Multiple Output (SIMO) techniques such as maximum ratio combining can be used to achieve diversity with multiple receive antennas.

Mode 2, also known as Transmit Diversity (TD), employs up to 4 transmit antennas along with space frequency block coding [12, p.69] to provide additional spatial diversity for the fading radio channel.

Channel Quality Indicator (CQI) feedback is provided for both modes, indicating which MCS out of 15 would achieve the highest throughput given the current channel state.

Open Loop Spatial Multiplexing

Open loop spatial multiplexing (OLSM) or transmission mode 3 is the simplest spatial multiplexing scheme in LTE. In addition to CQI feedback, it only relies on Rank Indicator (RI) feedback which signals the preferred number of spatial layers to the eNodeB.

Since RI and CQI depend merely on the SNR and the macro scale scattering environment than on the exact form of $\mathbf{H}$, OLSM can cope with rapid changes in the small scale fading environment and is thus suited for high mobility scenarios.

The lack of channel knowledge prohibits to choose a precoder specifically suited to $\mathbf{H}$: Instead, a codebook of unitary precoding matrices is cycled through in a periodic manner, effectively distributing the L layers equally among the N_{TX} transmit antennas. Besides this averaging effect, Cyclic Delay Diversity (CDD) [9] is employed to transform the spatial diversity into additional delay diversity [12, p.66] . The precoding matrix for subcarrier k is given by [4]

$$\mathbf{P}_k = \mathbf{W}_{k \bmod |\mathcal{W}_L|} \mathbf{D}_k \mathbf{U} \,, \tag{2.15}$$

where the $N_{\mathrm{TX}} \times L$ matrix $\mathbf{W}_{k \bmod |\mathcal{W}_L|}$ is selected from a rank dependent codebook $\mathcal{W}_L$ in a cyclic manner and changes from subcarrier to subcarrier, similar to the $L \times L$ diagonal matrix $\mathbf{D}_k$ introducing the CDD. The constant $L \times L$ matrix $\mathbf{U}$ averages out the channel differences as seen by the L layers. For example, for two transmit antennas and $L = 2$ we have

$$\mathcal{W}_2 = \{\mathbf{W}_0\} = \left\{ \frac{1}{\sqrt{2}} \begin{bmatrix} 1 & 0 \\ 0 & 1 \end{bmatrix} \right\}, \quad \mathbf{D}_k = \begin{bmatrix} 1 & 0 \\ 0 & \mathrm{e}^{-\mathrm{j}2\pi k/2} \end{bmatrix}, \quad \mathbf{U} = \frac{1}{\sqrt{2}} \begin{bmatrix} 1 & 1 \\ 1 & \mathrm{e}^{-\mathrm{j}2\pi/2} \end{bmatrix}. \tag{2.16}$$

Closed Loop Spatial Multiplexing

Closed Loop spatial Multiplexing (CLSM) or mode 4 extends the RI and CQI feedback of OLSM by Precoding Matrix Indicator (PMI) feedback, signaling back the preferred precoder by means of a codebook index. In that way, gains can be achieved compared to OLSM if the channel $\mathbf{H}$ changes slowly enough. [30] presents an approach for selecting the precoder $\mathbf{P}_i$, $i = 1, \ldots, |\mathcal{P}|$ from a codebook $\mathcal{P}$ based on maximizing the aggregate RB post-equalization mutual information:

$$\mathbf{P} = \arg\max_{\mathbf{P}_i \in \mathcal{P}} \sum_{k=1}^{N_{\text{sc}}^{\text{RB}}} \sum_{n=1}^{N_{\text{sym}}^{\text{RB}}} I_{n,k}(\mathbf{P}_i)\,, \tag{2.17}$$

where the mutual information per RE is given by

$$I_{n,k} = \sum_{\nu=1}^{L} \log_2(1 + \text{SINR}_{n,k,\nu})\,. \tag{2.18}$$

For a linear receiver resolving the N_{RX} receive streams to L layers by means of a $L \times N_{\text{RX}}$ matrix $\mathbf{F}_{n,k}$,

$$\mathbf{r}_{n,k} = \mathbf{F}_{n,k}\mathbf{y}_{n,k} = \underbrace{\mathbf{F}_{n,k}\mathbf{H}_k\mathbf{P}}_{\mathbf{K}_{n,k}}\mathbf{x'}_{n,k} + \mathbf{F}_{n,k}\mathbf{z}_{n,k} \tag{2.19}$$

the post-equalization Signal to Interference plus Noise Ratio (SINR) on RE (n, k, ν) is given by

$$\text{SINR}_{n,k,\nu} = \frac{|\mathbf{K}_{n,k}(\nu,\nu)|^2}{\sum_{i \neq \nu} |\mathbf{K}_{n,k}(\nu,i)|^2 + (\sigma_z^2 + \text{MSE}_{n,k}) \sum_i \mathbf{F}_{n,k}(\nu,i)}, \tag{2.20}$$

where $\mathbf{K}_{n,k}(\nu,i)$ is the element in row ν and column i of the matrix $\mathbf{K}_{n,k}$ and $\text{MSE}_{n,k}$ denotes the Channel Estimation Mean Squared Error (MSE).

2.4.2 MU-MIMO Modes

Reconsider Equation (2.12). Suppose that UE $u \in \{1, 2, \ldots, N_{\text{UE}}\}$ has $N_{\text{RX},u}$ receive antennas and is scheduled on $L_u \leq N_{\text{RX},u}$ layers, which are mapped to the N_{TX} transmit antennas via the $N_{\text{TX}} \times L_u$ precoding matrix $\mathbf{P}_u$. For that case, Equation (2.11) can be generalized to

$$\mathbf{y} = \mathbf{HPx'} = \begin{bmatrix} \mathbf{H}_1 \\ \mathbf{H}_2 \\ \vdots \\ \mathbf{H}_{N_{\text{UE}}} \end{bmatrix} \begin{bmatrix} \mathbf{P}_1 & \mathbf{P}_2 & \ldots & \mathbf{P}_{N_{\text{UE}}} \end{bmatrix} \begin{bmatrix} \mathbf{x'}_1 \\ \mathbf{x'}_2 \\ \vdots \\ \mathbf{x'}_{N_{\text{UE}}} \end{bmatrix} = \begin{bmatrix} \mathbf{y}_1 \\ \mathbf{y}_2 \\ \vdots \\ \mathbf{y}_{N_{\text{UE}}} \end{bmatrix}. \tag{2.21}$$

Thus, the receive vector without noise for UE u is given by

$$\mathbf{y}_u = \overbrace{\mathbf{H}_u\mathbf{P}_u\mathbf{x'}_u}^{\text{desired signal}} + \overbrace{\sum_{i\neq u}\mathbf{H}_u\mathbf{P}_i\mathbf{x'}_i}^{\text{interference}} . \tag{2.22}$$

Hence, the UE cannot compute a post-equalization SINR similar to Equation (2.20) as it does not know the interference term in Equation (2.22). Consequently, it is unable to autonomously determine the CQI and precoder in an optimal way. As a result, different feedback strategies are required, which will be presented in the following.

Codebook based MU-MIMO

For $L_u = N_{\mathrm{RX},u} = 1$, $\forall u$, Equation (2.22) simplifies to

$$y_u = \mathbf{h}_u^T\mathbf{p}_u x'_u + \sum_{i\neq u}\mathbf{h}_u^T\mathbf{p}_i x'_i . \tag{2.23}$$

A codebook based scheme can be implemented as follows: The UEs selects

$$\mathbf{p}_u = \arg\max_{\mathbf{p}_i\in\mathcal{P}}\langle\mathbf{p}_i, \mathbf{h}_u\rangle \tag{2.24}$$

as a precoder, computes a CQI value neglecting the interference term in Equation (2.22) and signals PMI and CQI back to the eNodeB. The transmitter then co-schedules the UEs that introduce the least interference, i.e., for which $\langle\mathbf{p}_i, \mathbf{p}_j\rangle$, $i, j \in \{1, \ldots, N_{\mathrm{UE}}\}$, $i \neq j$ is minimized and corrects the reported CQI by the residual interference. A similar approach can also be used for $1 \leq L_u \leq N_{\mathrm{TX},u}$.

In LTE Release 8, mode 5 has been specified to support such a codebook based MU-MIMO scheme. While this approach works with the same feedback mechanism as mode 4, its performance is limited by the granularity of the codebook [14]. To overcome this short coming, LTE-A Release 10 [4] defined a new RS structure [24, 29] along with transmit mode 9. Mode 9 still relies on codebook based precoding, but the granularity of the codebook is increased by using two PMI feedback values for 8 transmit antennas. The new RS structure allows for transparent precoding and thus for dynamic switching between MU-MIMO and SU-MIMO [21].

[21] also presents system level simulation results, indicating that the two-way LTE-A codebook achieves the desired improvement in comparison to the LTE codebook and almost reaches the performance of non codebook based schemes. The results are however optimistic in assuming that there is a sufficient amount of UEs so that a set of orthogonal users can be found.

Non codebook based MU-MIMO

If the number of active UEs is limited, non codebook based schemes such as ZF beamforming [28] and block diagonalization [32] have to be used to cancel the interference between UEs. As mentioned in Chapter 1, LTE is a constantly evolving mobile communication standard. The Release 10 RS structure sets the stage for non codebook based schemes, but an according feedback mechanism is not defined yet[6]. [31] presents a ZF beamforming scheme based on Channel Vector Quantization (CVQ), where N_{UE} single antenna UEs feed back their normalized and quantized channel direction $\hat{\mathbf{h}}_u$ and the eNodeB then computes the zero forcing precoder

$$\mathbf{P} = \mathbf{G}(\mathcal{U})\mathrm{diag}(\mathbf{p})^{1/2} = \hat{\mathbf{H}}(\mathcal{U})^H \left(\hat{\mathbf{H}}(\mathcal{U})\hat{\mathbf{H}}(\mathcal{U})^H\right)^{-1} \mathrm{diag}(\mathbf{p})^{1/2} \tag{2.25}$$

where $\mathcal{U}$ denotes the set of selected UEs and $\hat{\mathbf{H}}(\mathcal{U}) \in \mathbb{C}^{|\mathcal{U}| \times N_{\mathrm{TX}}}$ denotes the composite quantized channel. The elements

$$p_i = \frac{P}{|\mathcal{U}| \ \|\mathbf{g}_i\|^2} \tag{2.26}$$

of $\mathbf{p}$ equally distribute the transmit power P amongst the users and $\mathbf{g}_i$ is the i-th column of $\mathbf{G}(\mathcal{U})$.

Measurements results of such a scheme are presented in [27], using the software developed in course of this thesis. While the receiver is still the same multi antenna receiver described in Section 3.1.2, the 4 receive antennas are treated as individual UEs having only knowledge about their own $1 \times N_{\mathrm{TX}}$ channel. The scenario can be interpreted as four UEs located in the same room, experiencing similar signal strength but different small scale fading.

[6] The most recent LTE-A Release 11 [5] , which is still being specified, introduces an additional transmission mode 10. Similar to mode 9, mode 10 will be a versatile mode supporting up to 8 layers using UE-RS and is targeted for coordinated beamforming in CoMP scenarios. [5, 8].

Chapter 3

The Vienna MIMO Testbed

The Vienna MIMO Testbed is a distributed set of measurement hardware that enables the transmission of arbitrary mobile radio signals with a bandwidth of up to 20 MHz over the air. It currently consists of one indoor receiver, three identical rooftop transmitters and the infrastructure to interconnect, synchronize and monitor those components. Figure 3.1 depicts a schematic overview of the testbed hard- and software. Section 3.1.1 and Section 3.1.2 describe the transmitter and receiver hardware in more detail.

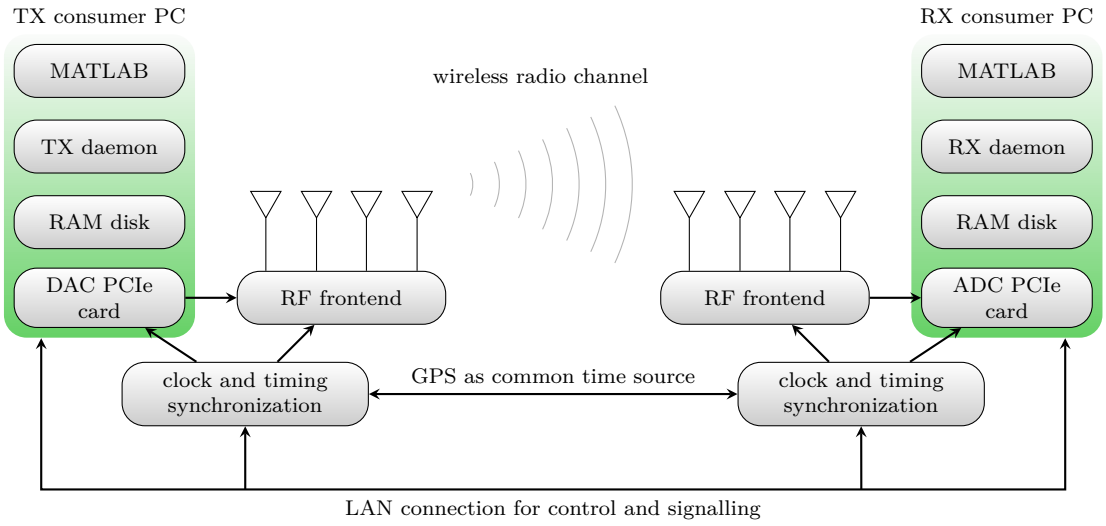

Figure 3.1: Working principle of the Vienna MIMO Testbed

3.1 Hardware

The three transmitters, referred to as TX1, TX2 and TX3 are located at different sites at the Vienna University of Technology. Figure 3.3 depicts the rooftop antenna connected

to TX1, which was used for the measurements in Chapter 5. In contrast, the receiver RX4 is located indoors, as depicted in Figure 3.2.

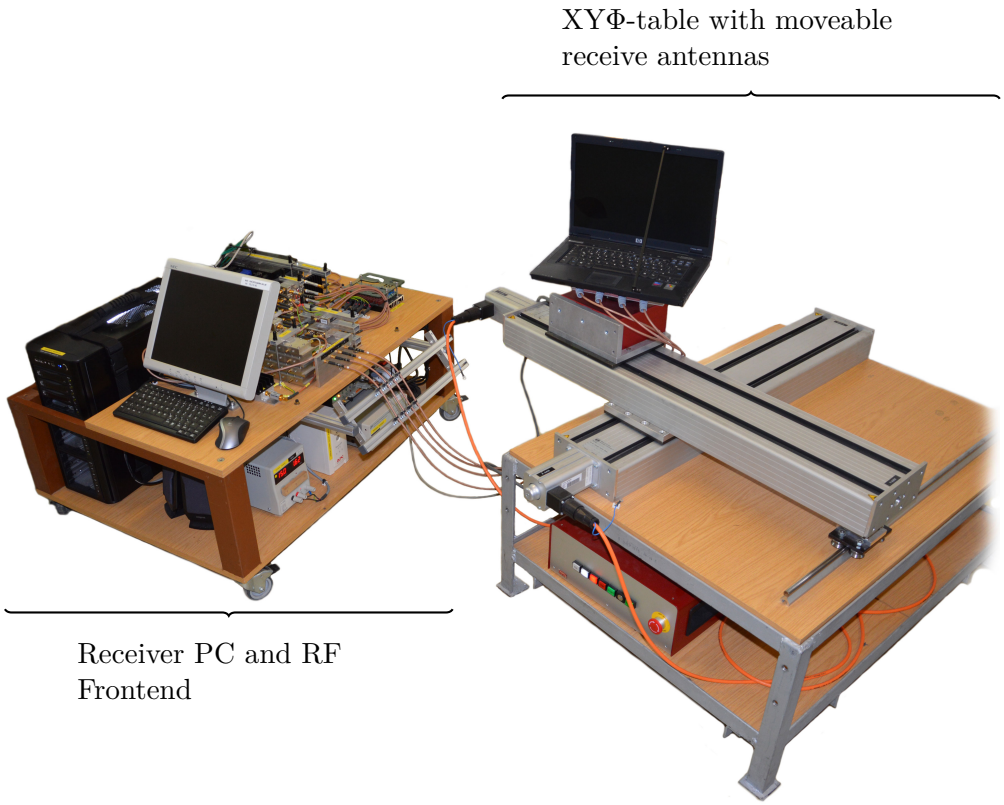

Figure 3.2: Indoor revceiver RX4

3.1.1 Transmitter Hardware

Consumer grade PC

A computer built with off-the-shelf components (Intel Core i7 CPU, Asus Mainboard, up to 24 GByte RAM) housing the Innovative Integration X5-TX DAC card. This card features four 16 Bit DAC channels with a (for our implementation) fixed sampling rate of 200 Msamples/s and is connected to the PC via PCIe bus. The PC is running a server software called `TX Daemon`, which —amongst other tasks— takes care of reading data from disk to the DAC card, cf. Section 3.2.1.

RF frontend and power amplifiers

The RF frontend features 4 synchronous RF chains consiting of an upconverter, various filters, a digitally programmable attenuator, and power amplifiers. The input to this functional block is the output from the DAC card which is already digitally upconverted to an Intermediate Frequency (IF) of 70 MHz. The output is the upconverted, filtered and amplified radio signal at a carrier frequency $f_c = 2.5$ GHz, which is fed to the transmit antennas. For a detailed description, the reader is referred to [10, 17].

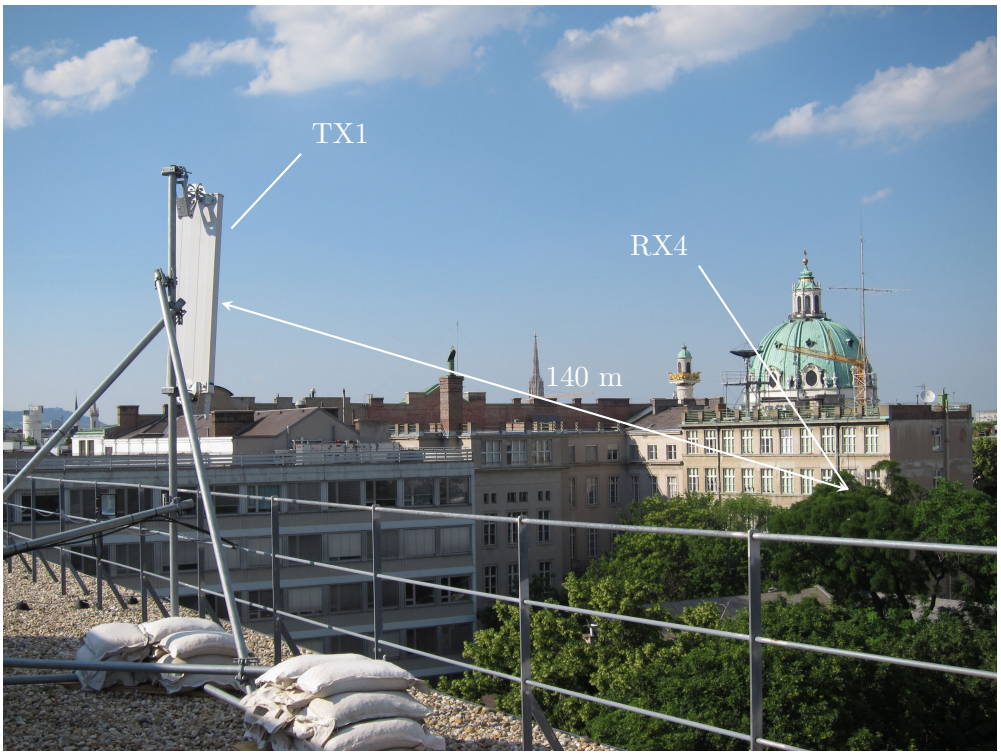

Figure 3.3: Rooftop transmitter TX1 with Kathrein 80010543 XX-pol antenna [6] used for the measurements in Chapter 5. The baseband hardware and RF frontend of TX1 look similar to those of RX4 and are located indoors.

Antennas

The outputs of the RF-chain can be connected to different types of antennas, e.g., the Kathrein 80010543 XX-pol antenna [6] mounted on the rooftops of the technical university for urban outdoor-to-indoor measurements or the Kathrein 80010677 antenna [7] for pico cell indoor-to-indoor measurements. Mixed scenarios are also possible since there are three identical transmitters available, allowing for an up to 12×4 MIMO setup.

GPS-Device and Rubidium Frequency Standard

Each transmitter has its own GPS receiver as well as a rubidium frequency standard for clock synchronization. An uninterruptible power supply guarantees a stable an precise clock signal, even in case of short temporal power outages.

Timing Synchronization Unit

Hardware based timing synchronization is achieved using the unit developed in [13]. More over, the synchronization unit has an RS232 output port which can be connected to stepper motor controllers.

Sensor PC

In addtition to the consumer grade PC, a small form factor PC is used for monitoring environmental conditions and controlling USB power switches. It is connected to a variety of different sensors, e.g., fog, rain and temperature and can be used to power on and off individual parts of the transmitter, such as RF components, power amplifiers, webcams and floodlights.

3.1.2 Receiver Hardware

Consumer grade PC

Similar to the transmitter, the receiver includes a consumer grade PC containing a X5-RX ADC card featuring four 16 Bit ADC channels with a (in our implementation) fixed sampling rate of 200 Msamples/s. The PC is running a server software called `RX Daemon`, which —amongst other tasks— takes care of writing data from the ADC card to disk, cf. Section 3.2.1.

RF frontend and power amplifiers

This functional block gets the received antenna signal at carrier frequency $f_c = 2.5$ GHz as input an outputs a signal that is filtered, amplified and downconverted to 70 MHz to the ADC card. Similar to the transmitter RF frontend there are four synchronous RF chains. For more detailed information, the reader is referred to [10, 16].

Receive Antennas and XYΦ-table

The receive antennas are integrated in a Notebook PC which is mounted on a XYΦ-table, cf. Figure 3.4. This setup allows for producing various MIMO channel realizations by moving and rotating the receive antennas to a different physical location where they experience a different small scale fading environment.

GPS-Device and Rubidium Frequency Standard, Timing Synchronization Unit and the Sensor PC

Those components are identical to the transmitter hardware, cf. Section 3.1.1.

3.2 Software

3.2.1 Daemon Software

All the hardware described in the previous section wants to be controlled and coordinated. Ideally, low-level programming should be avoided completely when carrying out measurements, allowing the researcher to focus on the signal processing rather than on hardware details. For that reason, a light-weight, fast piece of software is required

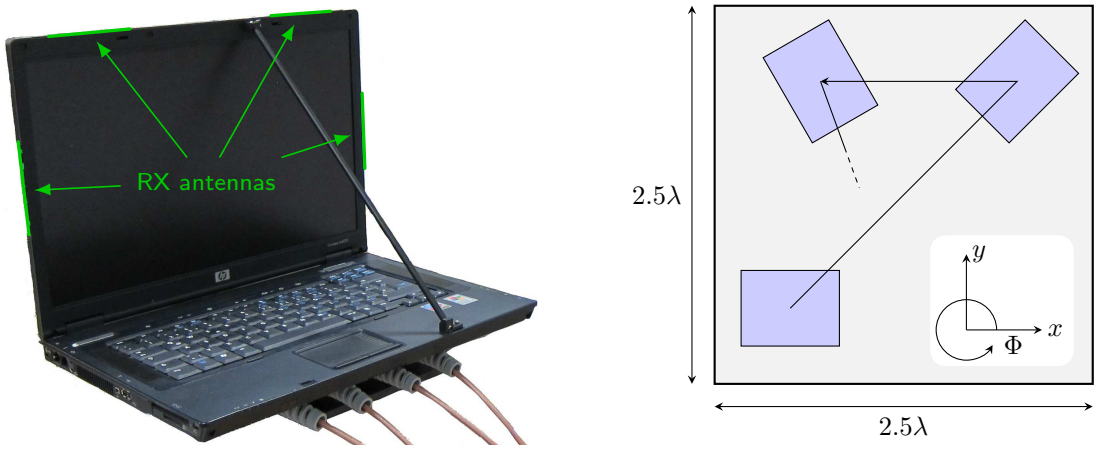

(a) (b)

Figure 3.4: Notebook PC containing 4 receive antennas (a). The laptop is mounted on an XYΦ-table, which changes the notebook's position (x, y) and orientation Φ in order to allow for measurements with independent channel realizations (b)

```
1 xmUDP_send(pointer, ip, port, uint8("Command"));
2 RXmeassage = xmUDP_receive(pointer, timeout);
```

Listing 3.1: MATLAB functions calls to interact with the daemon software. The call of `xmUDP_send()` sends the command `Command` to a daemon listening on the socket `ip:port`, where `pointer` identifies the local process socket. Similarly, `xmUDP_receive()` waits until `timeout` for a message which, upon reception, is assigned to the variable `RXmeassage`. Strictly speaking, received messages are handled by the operating system which saves them to a buffer if the respective port is opened, before they are read out by `xmUDP_receive()`. Both functions are realized as .mex functions utilizing the Windows Socket API. For a thorough description of the commands applicable to the `TX` and `RX daemon` software, the reader is referred to [17] and [16], respectively.

serving as a layer of abstraction between hardware and higher layer MATLAB programs used for generating and evaluating signals.

The `TX daemon` and `RX Deamon` developed in [16, 17] have been designed to meet this requirement. They are written in C++ employing programming libraries of the DAC/ADC card vendor. In particular, they control the data flow from the ADC card to disk and from disk to the DAC card. Most importantly, the type of signal (HSDPA, LTE, ...) is transparent to the daemons. Both `TX Daemon` and `RX Daemon` are realized as server programs, i.e., they bind to a socket on the transmit and receive PC and await instructions passed on to them via UDP packets. A MATLAB script can then interface the daemons with functions as given in Listing 3.1.

Originally, the daemons have been designed for the brute force approach described in Chapter 1. Hence, they have been optimized for fast reading and writing of huge amounts of data to RAID arrays. However, the feedback based approach presented in this thesis does not need to transmit an exhaustive set of signals. Consequently, a reduction of the retransmission delay can be achieved if the daemons are configured to

read and write data from a RAM disk.

3.2.2 Matlab Software

As indicated in Figure 3.1, the MATLAB program generating and evaluating the signal resides one logical layer above the daemon software. For the brute force approach [23], the MATLAB layer consists of the Vienna LTE Link-Level Simulator [22] supplemented by a script to generate signals and a cluster software developed in [15]. The cluster software allows to distribute the receive signals to multiple PCs for evaluation, using functionality of the LTE Link Level Simulator for the actual decoding process.

In order to allow for real-time feedback, an alternative MATLAB layer has been developed for this thesis, while the underlying functionality of the testbed remains unchanged. Chapter 4 describes the tasks that such a program has to fulfill and presents details of the implementation.

Chapter 4

Measuring with real-time feedback

In real world systems, feedback information is usually calculated and fed back in a periodic manner with a fixed time T_f between two consecutive feedbacks. The feedback algorithms are optimized and executed "in hardware" on so called Application specific integrated circuits (ASICs); thus the execution time of the algorithms is of minor concern. The limiting factors are the feedback overhead on the uplink channel and the amount of resources reserved for pilot symbols on the downlink. The LTE-A standard specifies T_f to be 5, 10, 40 or even 80 ms [3, p. 90].

In signal processing research however, algorithms are typically written in a high-level programming language such as MATLAB to speed up the development and abstract hardware details like memory management. Thus, the execution time of the MATLAB program is crucial when it comes to minimizing the feedback delay. In that sense, we define "real-time" as achieving a fast enough retransmission so that the channel change does not affect the CSI feedback. (cf. Chapter 5).

For that reasons, the procedure depicted in Figure 4.1 has been chosen. First of all, a pilot frame which is used for channel- and SNR estmation is transmitted. These estimates are then used to calculate the feedback and generate the transmit signal accordingly. Finally, the frames incorporating the feedback are sent, followed by another pilot frame to quantify the channel change during one measurement.

Section 4.1 provides more detailed information on how the feedback is defined and calculated. Subsequently, Section 4.2 treats the exact temporal course of events and elaborates processing steps constituting the delay . Eventually, Section 4.3 concludes this chapter with an overview of the MATLAB implementation of the measurement and simulation environment.

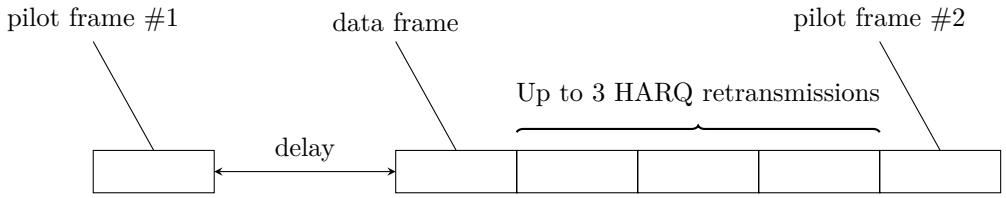

Figure 4.1: Time schedule for one measurement. The above procedure is carried out for any transmit power value and any XYΦ-table position. Only pilot frame #1 is processed online, where as the other received frames are decoded offline by the `Evaluate.m` MATLAB program, cf. Section 4.3.

4.1 Feedback definition and calculation

As we have seen in Chapter 2, LTE supports adaptive modulation and coding as well as spatial preprocessing in the form of linear precoding. Consequently, the transmitter needs to know what MCS, rank and precoder would be the best choice given the current channel state. Neglecting the time-dependence of the feedback process[1] , one can define a generic LTE feedback function as follows:

$$\begin{bmatrix} \text{PMI} \\ L \\ \text{CQI} \end{bmatrix} = \mathbf{f}(\text{SNR}, \hat{\mathbf{H}}, \text{MSE}) \tag{4.1}$$

As before, PMI is the index of the preferred precoder, L is the preferred rank and the CQI determines the MCS. The inputs of this function are continuous quantities known at the receiver by means of pilot based channel estimation. On the other hand, the outputs are discrete codebook related numbers constituting the LTE feedback to be transmitted on the uplink channel. The channel estimation MSE expresses the uncertainty that the receiver has about its estimated channel knowledge and is in general not known. It can be computed analytically as a function of the channel correlation, SNR and inter carrier interference power [25], but unfortunately neither of these quantities is known at the receiver as well. There is however a way to obtain an estimate of it, as will be shown in Section 4.2.3.

For a noncodebook based scheme like the ZF beamforming scheme decribed in Section 2.4.2, the generic input-output relation

$$\begin{bmatrix} \hat{\mathbf{h}}_{\text{quant}} \\ \text{CQI} \end{bmatrix} = \mathbf{g}(\text{SNR}, \hat{\mathbf{h}}, \text{MSE}) \tag{4.2}$$

substitutes the codebook based PMI with the quantized version of the channel $\hat{\mathbf{h}}_{\text{quant}}$.

For the feedback functions, we used the `LTE_feedback()` function of the LTE-A simulator [22]. It essentially computes the per-RE SINR Equation (2.20) for all possible

[1] As the channel is correlated over time, so is the feedback. Sophisticated algorithms can make use of this by viewing the feedback as a stochastic process over time, trying to predict the channel state until new feedback arrives [31].

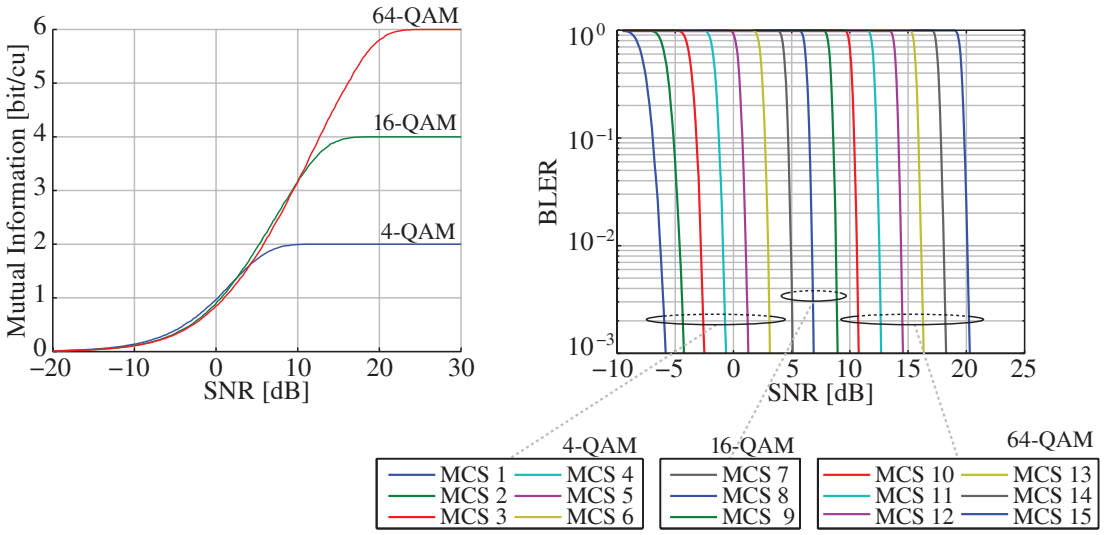

Figure 4.2: Left: BICM capacities in bits per channel use for 4-, 16-, and 64 QAM. The BICM capacities are calibrated with MCS dependend factors, yielding as many SINR-to-MI mappings as there are MCSs. Right: Simulated AWGN block error rate curves for the 15 MCS defined in LTE. Figure taken from [18]

precoders and ranks. Subsequently, the SINRs are mapped to the Mutual Information (MI) domain using BICM [11]. In this domain, the MI is averaged over one RB and the average MI is transformed back to the SINR domain, yielding an equivalent AWGN SNR per RB. Using block error rate over SNR mappings, the highest[2] MCS achieving a block error rate below 0.1 is selected. At the end of this brute force procedure, there is one triple $(\mathrm{PMI}, L, \mathrm{CQI})$ maximizing spectral efficiency at a block error rate below 0.1. The BICM capacities as well as the block error rate curves are depicted in Figure 4.2.

For the MU-MIMO case the SINR is not known at the receiver. Thus, the CQI output of Equations (4.1) and (4.2) needs to be revised downwards by the eNodeB.

4.2 The measurement procedure

As indicated in Chapter 3, the `RX daemon` saves the receive signal, which arrives at the ADC card at an IF of 70 MHz and is then sampled with 200 Msamples/s, to RAM disk. Similarly, the `TX daemon` expects a signal with the same sampling rate which is already digitally upconverted to the same IF. Thus, in coherence with Figure 2.3, the following tasks have to be performed to extract the feedback information from the receive pilot frame #1 and generate a new transmit file accordingly:

1. Downconversion of the receive samples from the IF $f = 70\mathrm{MHz}$ to the complex baseband (cf. Section 4.2.2)

2. Downsampling from 200 Msamples/s to the bandwidth dependent sampling rate $f_s = K_{\mathrm{FFT}}/T$ (cf. Equations (2.3) and (2.14) and Section 4.2.2)

[2] in terms of spectral efficiency

3. Removal of the cyclic prefix and performing an FFT to transform the receive signal to the frequency domain
4. Channel- and SNR estimation (cf. Section 4.2.3)
5. Feedback calculation according to Equations (4.1) and (4.2)
6. Conveying the feedback information back to the transmitter (cf. Section 4.2.1)
7. Resource allocation and scheduling (cf. [27])
8. Coding and symbol mapping (cf. Section 4.2.4)
9. Precoding and computing the IFFT
10. Upsampling and upconversion, i.e., the inverse operations to step 1 and 2

Each of these steps adds to the total delay as defined in Figure 4.1 and is described in the following.

4.2.1 The feedback link

As discussed in Figure 3.1, the testbed components are connected via a Local Area Network (LAN) for signaling purposes. In case of the connection from TX1 to RX4, the LAN is realized as single mode fiber providing a Gigabit Ethernet connection between transmitter and receiver. Transmitting back the entire receive pilot frame #1 (cf. Figure 4.1) and evaluating Equations (4.1) and (4.2) at the transmitter has thus been preferred to evaluating Equations (4.1) and (4.2) at the receiver and signaling back the outputs of $\mathbf{f}(\cdot)$ or $\mathbf{g}(\cdot)$. Since the receive pilot frame is only about 4.6 MB in size, this approach does not have significant impact on the total delay[3] and allows for more flexibility. As a result, a simple MATLAB script can be used to control and conduct the measurement, whereas distributed server software similar to the `TX` and `RX daemon` would be necessary otherwise.

4.2.2 Downconversion and Upconversion

The testbed operates at a fixed sampling frequency of $f_{\mathrm{TB}} = 200$ Msamples/s. The sample rate of the LTE signal depends on the channel bandwith via the number of subcarriers K, cf. Equation (2.3). More over, the RF frontends at the transmitter and the receiver feature an IF stage of 70 MHz. Consequently, the LTE signal needs to be digitally upsampled and upconverted to the IF before transmission and digitally downconverted and downsampled after the transmission.

[3] Transmitting 4.6 MB over a Gigabit ethernet link takes about 36 ms. The delay due to signal processing is at least one order of magnitude higher, depending on the transmission setup.

Upconversion and upsampling

First the discrete time transmit signal $s[m]$ (cf. Equation (2.4)) is padded with $q-1 = \lfloor T_s f_{\mathrm{TB}} \rfloor$ zeros between any two signal values to yield the signal $\tilde{s}[m]$ with decreased sampling time $\tilde{T}_s = T_s/q$. The subsequent lowpass interpolation is realized in the frequency domain by computing $\tilde{S}_k = \mathrm{FFT}_{m\to k}(\tilde{s}[m])$ and applying an ideal lowpass in the frequency domain, i.e., zeroising non baseband frequency components in $\tilde{S}_k$. After that, the upconversion amounts to a simple cyclic shift of the frequency domain signal, followed by an IFFT to obtain the complex valued transmit signal, whose real part is sent off from the DAC card to the RF stage.

Downconversion and downsampling

The receive samples originating from the ADC card are transformed to the frequency domain, shifted to baseband and low pass filtered in the frequency domain. Afterwards, the signal is transformed back to the time domain and resampled using every q-th sample and dumping the samples in between.

4.2.3 SNR- and channel estimation

In order to calculate the feedback as defined in Equations (4.1) and (4.2), the channel state $(\mathbf{H}, \sigma_z^2)$ has to be estimated. Taking into account the inevitable channel estimation error in real world measurements, the unknowable perfect CSI $(\mathbf{H}, \sigma_z^2)$ can be replaced by $(\hat{\mathbf{H}}, \sigma_z^2, \mathrm{MSE})$, where the channel estimation MSE is given by

$$\mathrm{MSE} = \frac{1}{N_{\mathrm{TX}} N_{\mathrm{RX}}} \sum_{i=1}^{N_{\mathrm{RX}}} \sum_{j=1}^{N_{\mathrm{TX}}} \mathrm{E}\Big\{ |H_{i,j} - \hat{H}_{i,j}|^2 \Big\} = \mathrm{E}\Big\{ \|\mathbf{H} - \hat{\mathbf{H}}\|_{\tilde{F}}^2 \Big\}, \tag{4.3}$$

with $\| \cdot \|_{\tilde{F}}$ denoting the Frobenius norm divided by the square root of the product of the matrix dimensions. In case of deterministic knowledge of $\mathbf{H}$ and $\hat{\mathbf{H}}$, the expectation operator amounts to an identity operation. However, Equation (4.3) still involves the channel and for the case of measurements, neither that nor its statistics are known at the receiver. To overcome this issue, a two way channel estimation approach has been chosen, as described in the following.

Channel estimation

For calculating the channel estimation MSE as well as for reference purposes, (nearly) perfect channel knowledge is desired. Because of that, a pilot subframe solely consisting of RSs is transmitted prior to the actual data subframe. Figure 4.3 depicts this dense pilot structure, employing time averaging to suppress the noise and interpolation over frequency in between the pilot subcarriers.

Superimposed on the RS structure in Figure 4.3 is the standard compliant C-RS structure for LTE or the CSI-RS structure for LTE-A. The channel estimation MSE is

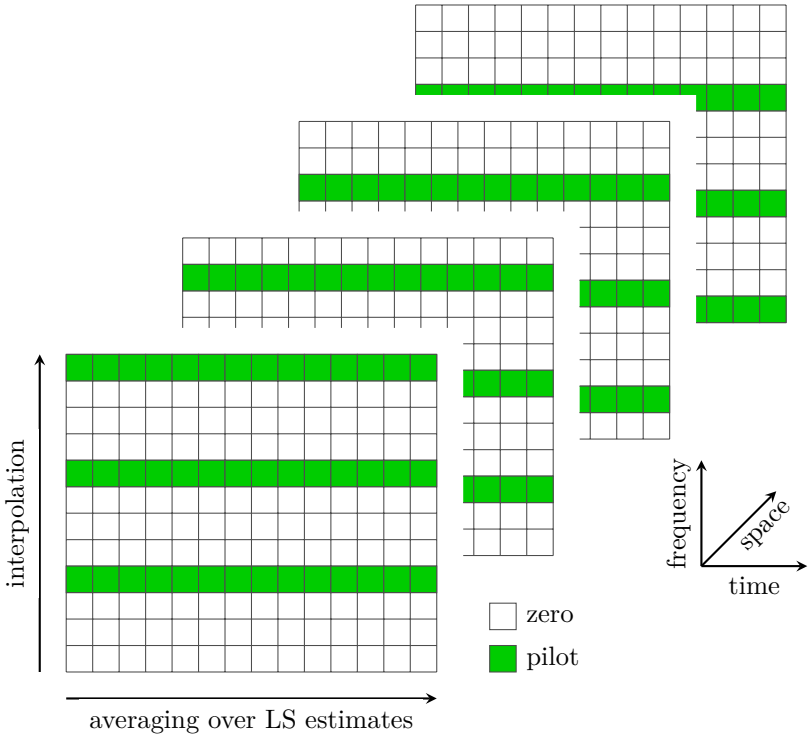

Figure 4.3: RS structure for obtaining a highly accurate estimate of the channel. Averaging over multiple OFDM symbols is employed, exploiting the quasi stationarity of $\mathbf{H}$. The more subframes are sent, the more symbols can be used for averaging but correspondigly more signal processing is necessary, increasing the retransmission delay. Averaging over N OFDM symbols increases the SNR on the pilot subcarriers by the factor N. In order to avoid interference between the antenna ports, only every N_{TX}-th subcarrier can be used.

then computed as the difference between the estimate obtained with the dense structure in Figure 4.3 and the estimate obtained with the standard compliant structure. Since both structures occupy disjoint sets of REs, the resulting MSE is over estimated:

$$\begin{aligned}\widehat{\mathrm{MSE}} &= \mathrm{E}\Big\{\|\mathbf{H}_{\mathrm{D}} - \mathbf{H}_{\mathrm{RS}}\|_{\tilde{F}}^2\Big\} = \mathrm{E}\Big\{\|(\mathbf{H}+\mathbf{E}_{\mathrm{D}}) - (\mathbf{H}+\mathbf{E}_{\mathrm{RS}})\|_{\tilde{F}}^2\Big\} \\ &= \tfrac{1}{N_{\mathrm{TX}}N_{\mathrm{RX}}}\mathrm{E}\Big\{\mathrm{tr}\big((\mathbf{E}_{\mathrm{D}} - \mathbf{E}_{\mathrm{RS}})^H(\mathbf{E}_{\mathrm{D}} - \mathbf{E}_{\mathrm{RS}})\big)\Big\} \\ &= \underbrace{\mathrm{MSE}_{\mathrm{D}}}_{\ll \mathrm{MSE}_{\mathrm{RS}}} + \mathrm{MSE}_{\mathrm{RS}} \approx \mathrm{MSE}_{\mathrm{RS}} = \mathrm{MSE}\end{aligned} \tag{4.4}$$

In this derivation, the channel estimate $\mathbf{H}_{\mathrm{D}}$ using the dense pilot structure and the channel estimate $\mathbf{H}_{\mathrm{RS}}$ using the standard compliant RS structure are expressed as sum of the true channel and error matrices $\mathbf{E}$, which are due to the noise on disjoint subcarriers and are therefore uncorrelated. Strictly speaking, Equation (4.4) is only valid on the pilot subcarriers, as it does not take into account the interpolation in between those positions. However, Figure 4.4 shows that Equation (4.4) is in general valid for channels with a large enough coherence bandwidth, where the interpolation error is negligible in comparison to the error caused by noise.

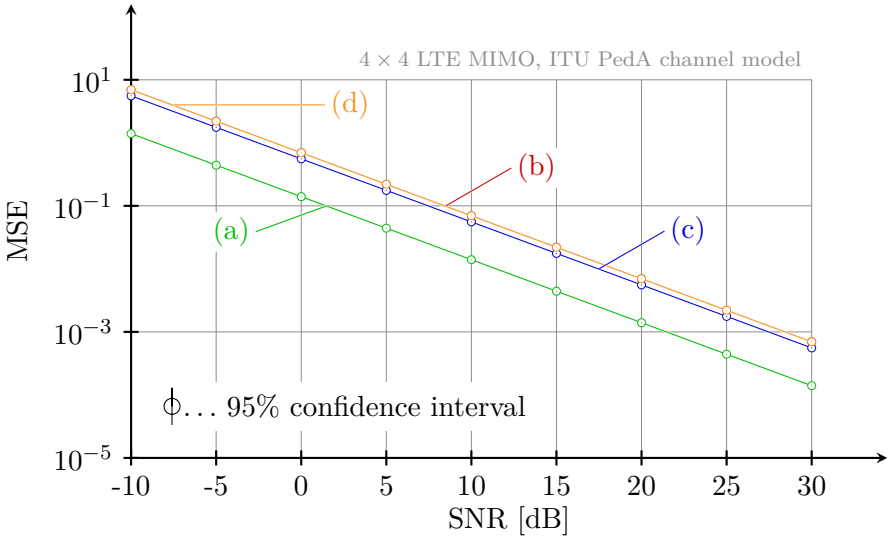

Figure 4.4: Channel estimation MSE simulation results for 4×4 LTE employing C-RS over an ITU PedA [20] channel. The MSE of the dense structure from Figure 4.3 (a) is about one order of magnitude smaller then the C-RS estimate (c). In coherence with Equation (4.4), the estimated MSE (d) perfectly matches (b), which is the sum of (a) and (c).

SNR estimation

Another quantity that has to be estimated to evaluate Equations (4.1) and (4.2) is the SNR. Since Equations (4.1) and (4.2) are sensitive to this variable, a highly accurate estimation in the frequency domain is carried out. Figure 4.5 depicts the pattern sent for the estimation process. Half of the transmitted REs carry symbols of magnitude $\sqrt{2P_{\mathrm{TX}}}$, where as the other half carries zeros. The signal power and noise power at receive antenna ν are then given by

$$P_{N,\nu} = \sum_{(n,k)\in\mathcal{N}} |y_{n,k,\nu}|^2 \,, \tag{4.5a}$$

$$P_{S,\nu} = \frac{1}{2}\left(\sum_{(n,k)\notin\mathcal{N}} |y_{n,k,\nu}|^2 - P_{N,\nu} \right) \,, \tag{4.5b}$$

with $\mathcal{N}$ denoting the set of zero subcarriers and $y_{n,k,\nu}$ being the receive symbol on RE (n,k,ν). The SNR at receive antenna ν SNR_ν and the total SNR are thus given by

$$\mathrm{SNR}_\nu = \frac{P_{S,\nu}}{P_{N,\nu}} \,, \tag{4.6a}$$

$$\mathrm{SNR} = \frac{\sum_{\nu=1}^{N_{\mathrm{RX}}} P_{S,\nu}}{\sum_{\nu=1}^{N_{\mathrm{RX}}} P_{N,\nu}} \,. \tag{4.6b}$$

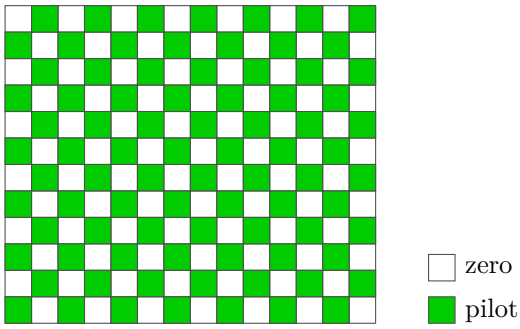

Figure 4.5: Transmit symbol pattern used for SNR estimation in the frequency domain. The total subframe with transmit power P_{TX} equally consits of zeros and symbols with magnitude $\sqrt{2}P_{\mathrm{TX}}$. On the zero REs, only noise is reveived where as on the other REs, double the signal power plus noise power is received.

4.2.4 Coding and symbol mapping

To keep the delay as small as possible, coding and symbol mapping is performed offline prior to the actual measurement. The basic idea is to generate an exhaustive set of datawords $\mathcal{D}$ (cf. Figure 2.3) for any possible number of RBs that the UE could be scheduled for. This set of datawords is then coded and mapped to modulation symbols for any possible MCS, yielding the set of symbol vectors $\mathcal{A}$. Taking into account HARQ retransmissions, we have

$$|\mathcal{A}| = |\mathcal{D}| N_{\mathrm{MCS}} (1 + N_{\mathrm{HARQ}}) \,, \tag{4.7}$$

where N_{MCS} is the number of MCSs and N_{HARQ} is the maximum number of HARQ retransmissions.

As an example, consider a system with 1.4 MHz bandwidth with $2N_{\mathrm{RB}} = 12$ RBs per TTI employing a SU-MIMO transmission scheme. For that case, there are 12 possible datawords, occupying from 1 up to 12 RBs. With $N_{\mathrm{MCS}} = 15$ and $N_{\mathrm{HARQ}} = 3$, 720 various length symbol vectors are generated. Upon the scheduling decision, the resource grid depicted in Figure 2.1 is filled with the pregenerated symbols. For the case of HARQ retransmissions N_{HARQ} additional subframes are filled with symbols representing the HARQ coded bits.

The set of symbol vectors $\mathcal{A}$, the set of datawords $\mathcal{D}$ and the set of codewords $\mathcal{C}$ only has to be generated once and can then be reused for multiple measurements. More over, $\mathcal{A}$ is small enough to fit in the RAM of the TX PC. Thus, the hard drives do not need to be accessed at all during a measurement, reducing the delay even further.

4.3 Software Overview

Figure 4.6 gives an overview of the measurement and simulation software. It mainly consists of 3 MATLAB scripts that share a common set of functions.

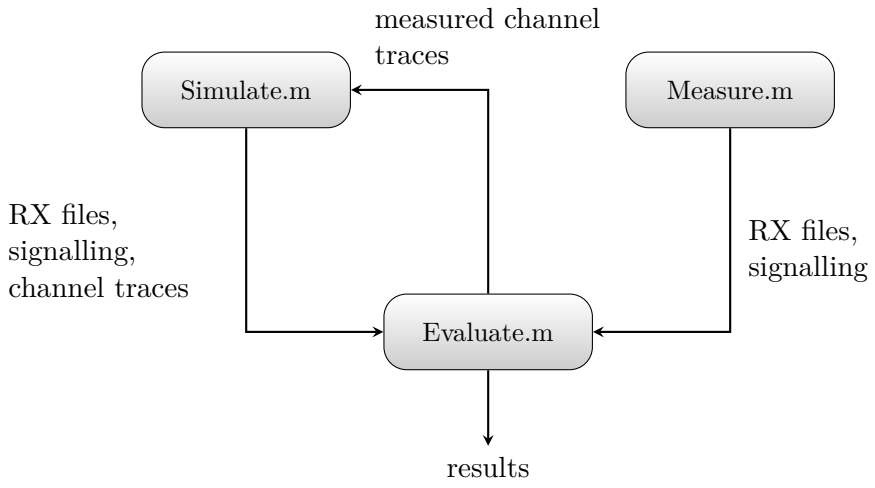

Figure 4.6: Software Overview

4.3.1 Measurement script

This script coordinates and conducts measurements with the testbed. It interfaces with the lower level `TX daemon` and `RX daemon` (cf. Section 3.2.1) programs via UDP commands. First of all, the LTE signal parameters are configured, the transmit power levels and positions of the XYΦ-table are configured and the pilot frames as described in Section 4.2.3 are generated. Subsequently, the script `InitializeTestbed.m` is called, which initializes, calibrates and resets the individual hardware components.

After this setup procedure, the actual measurement, as described in Algorithm 1 is conducted. The output of `Measure.m` are the receive files for any position and transmit

Algorithm 1 Measure.m

```
for all XYΦ-table positions do
  for all TX power levels do
    Set attenuators;
    Transmit pilot frame;
    Load ReceivePilotFrame;
    [channel, MSE, SNR] = evaluateCSI(ReceivePilotFrame);
    [DataSignal, signalling] = generateRTXframe(channel, MSE, SNR,
    LTEparams);
    Upconvert DataSignal;
    Transmit DataSignal;
    Save signalling;
  end for
end for
```

power as well as the `signalling`, which contains scheduling assignments and the CQI, PMI and RI feedback corresponding to the channel state.

4.3.2 Simulation script

The simualtion script is similar to the measurement script, except that no hardware control has to be performed and that the radio transmission is substituted with one of the baseband channel models implemented in [22]. The outputs are exactly the same as of `Measure.m`, the only exceptions being the simulated channels which are perfectly know and can thus be handed over to the evaluate script.

On top of the structural similarity to `Measure.m`, the scripts also share a common set of functions: e.g., `evaluateCSI()`, `generateRTXframe()` and others. Consequently, `Simulate.m` serves as a reference and can be used to compare measurements against simulations.

4.3.3 Evaluation script

The evaluation script attempts to demodulate and decode the receive files produced by `Measure.m` or `Simulate.m`. For that, it also needs to have access to the `signalling` parameters which are reflecting the channel state during the measurements

Chapter 5

Measurement based evaluation

5.1 Impact of the delay

In the previous chapter, the measurement sequence and the necessary signal processing for generating the data frame based on the received pilot frame have been described. All of this processing adds to the total delay in between which the mobile radio channel is subject to change.

In this section, we attempt to quantify the channel change and argue, that its effect is negligible on the measurements, i.e., that the same measurement results would be obtained if we had instantaneous channel knowledge rather than delayed one.

To quantify the change, we define

$$\Delta_k = \frac{\|\mathbf{H}_k^{(1)} - \mathrm{e}^{-\mathrm{j}\theta}\mathbf{H}_k^{(2)}\|_F^2}{\|\mathbf{H}_k^{(1)}\|_F \|\mathbf{H}_k^{(2)}\|_F} \tag{5.1a}$$

as the channel change between the transmission of pilot frame #1 and pilot frame #2 on subcarrier k (cf. Figure 4.1), with

$$\theta_k = \mathrm{mean}\Big(\arg\{\mathbf{H}_k^{(1)} \odot (\mathbf{H}_k^{(2)})^*\}\Big) \tag{5.1b}$$

being the average phase offset on subcarrier k.[1] The mean phase offset over all subcarriers and the mean channel change are then given by

$$\theta = \frac{1}{K}\sum_{k=0}^{K-1}\theta_k\,, \qquad \Delta = \frac{1}{K}\sum_{k=0}^{K-1}\Delta_k, \tag{5.1c}$$

respectively.

Before discussing the channel change, let us examine typical channel realizations obtained with a normalized receive signal. Figure 5.1a depicts the magnitude of the measured channel element $H_{2,1}$ both for an estimate obtained with pilot frame #1 and

[1] $\odot$ denotes the element-wise multiplication, $(\cdot)^*$ the complex conjugate and the mean$(\cdot)$ operation takes the sample mean over all matrix elements.

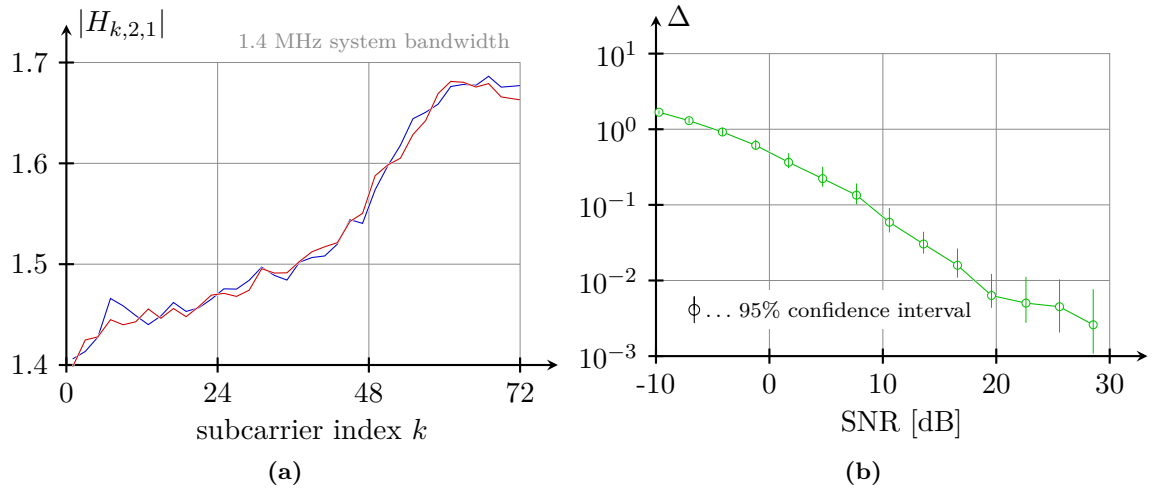

Figure 5.1: Two typical channel realizations for pilot frame #1 and #2 at high SNR (a) Measured channel change as defined in Equation (5.1) for the measurement as specified in Table 5.1 (b)

#2. The transmit power for this realization is 15 dBm, corresponding to a receive SNR of 34.43 dB; the delay between the two pilot frames is 472 ms. As we can see, the shape of the channel did not change during the measurement. The differences are merely due to the noisy estimate which we have to accept for small delays, cf. Figure 4.3. Considering that the channel state feedback is only calculated on an RB basis, we can safely argue that both channel realization would cause the same feedback. Indeed, as can be shown by feeding the measured channel traces to `Simulate.m`, both channel states yield the same result when inserted into Equation (4.1).

In coherence to that, Figure 5.1b shows the measured channel change Δ plotted over the average receive SNR. Until 20 dB SNR, the change is mainly due to the random differences of the noisy estimates, as can be concluded from the linear decrease in the doubly logarithmic plot. Above that level, Δ decreases slower with increasing variance around the sample mean, almost reaching 10^{-3}.

While these results are a good indicator, the question remains whether the delay affects the measured coded throughput. To answer that question, three different scenarios have been compared:

1. A measurement with an average retransmission delay of 467 ms. (Parameters in Table 5.1)

2. A simulation, using the channel traces at high SNR from the above measurement, i.e., a simulation reflecting the measured channel and the delay of the measurement

3. The same simulation as above, except using the same trace both for the pilot frame and the data frame, i.e., a simulation with with zero delay

The coded throughput results for all three scenarios are shown in Figure 5.2. As we can see, all scenarios perform approximately the same: The measurement is slightly below

the simulations, which are almost overlapping. Taking into account the close match between measurement and simulations as well as the fact that the zero delay simulation performs exactly the same as the simulation including the delay, we conclude that a zero delay measurement would perform within the confidence interval of the measurement with delay.

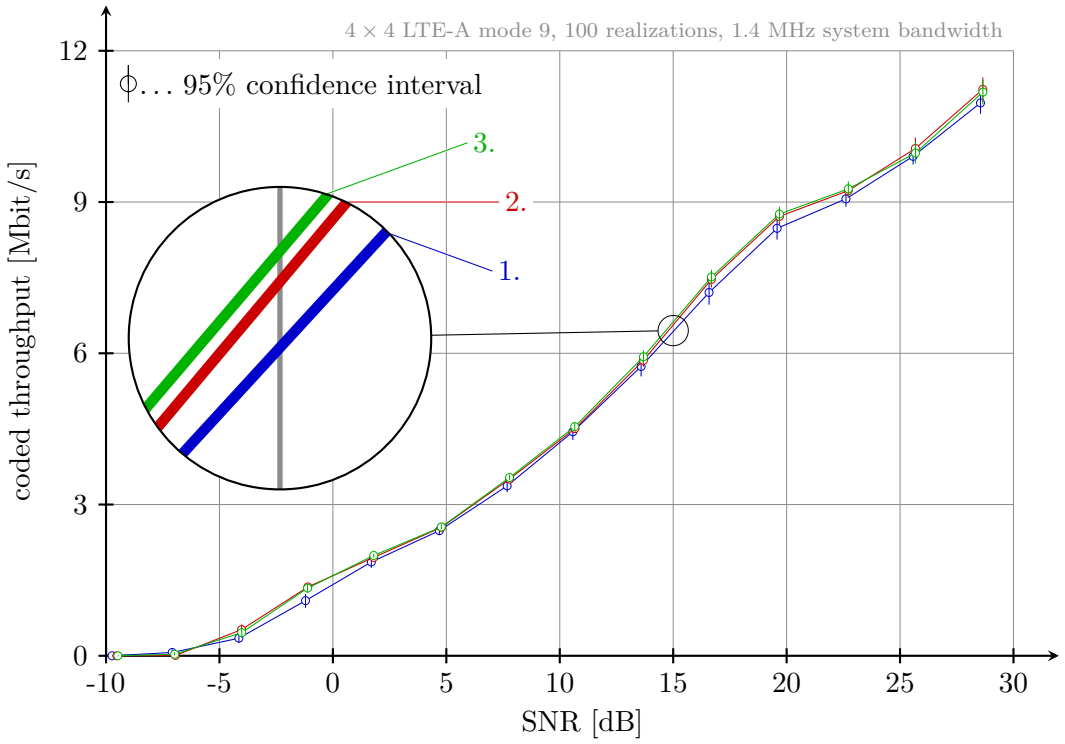

Figure 5.2: Comparison between a measurement and simulations based on measured channel traces

In general, the delay increases with the bandwidth of the LTE signal under investigation, as many processing steps presented in Chapter 4 scale with bandwidth (FFT, IFFT, feedback calculation, channel estimation, precoding, ...). However, the computationally expensive upconversion, upsampling, downconversion and downsampling are bandwidth independent and constitute a big part of the delay. For different system bandwidths between 1.4 MHz and 10 MHz, delays between 400 and 900 ms have been observed, which is about a factor of 5 to 10 times longer than the maximum standard compliant delay of 80 ms. While intuitively being a much too long delay for the term "real-time", it seems that the stationarity of the measurement setup (cf. Chapter 3) as well as the RB granularity of the feedback justify the denomination in the context of this thesis. More over, the higher order MIMO modes of LTE are meant to be used in static scenarios (cf. Table 2.2), rendering the conditions of the measurement as a typical application scenario rather than an artificial environment that only applies to the measurements.

5.2 Measurement vs. Simulation

After having demonstrated the self consistency of the measurement and simulation environment and discussing the feedback delay, this section devotes to setting the measurement results in context to simulation results obtained using baseband channel models. In addition, the effect of the feedback function is shown.

Figure 5.3 compares coded throughput simulation results obtained with `Simulate.m` with the measurement of the previous section. For the channel model, the ITU PedA model [20] has been chosen because its large coherence bandwidth matches the conditions of the measurement setup. As we can see, the measurement and the simulation yield a similar result for a large range of receive SNR form -10 up to 20 dB. Above that level, the curves diverge because the simulation assumes a spatially perfectly uncorrelated channel, achieving rank 4 transmission beyond 20 dB, whereas for the measurement the average rank does not exceed 3.5. This effect is due to the correlation between transmit and receive antennas in the real world measurement, decreasing the transmission rank on average.

Besides that, Figure 5.3 shows simulated curves that would have been achieved with optimal CQI feedback, i.e., if N_{pos} denotes the number of realizations and $D(\text{MCS}, \text{SNR})$ is the coded throughput achieved with a fixed MCS at a given SNR, then the throughput using optimal CQI feedback is given by

$$D(\text{SNR}) = \frac{1}{N_{\text{pos}}} \sum_{n=1}^{N_{\text{pos}}} \max_{\text{MCS}} D(\text{MCS}, \text{SNR}). \tag{5.2}$$

Equation (5.2) is actually only a fair comparison if all channel and noise realizations are the same for any CQI, which can only be guaranteed in simulations. For both the measurement and the simulation discussed in the previous paragraph, the optimal feedback curves are plotted in Figure 5.3, where the curve for the measurement is obtained by feeding the measured channel traces to `Simulate.m`. In case of the simulation using the PedA channel model, both curves match for low SNR, diverge for medium high SNR and are converging again for very high SNRs. In contrast to that, the optimal CQI curve based on the measured trace is always above the measured curve and even exceeds the optimal CQI simulated curve. This phenomenon can be understood by having a look at the average receive SNR as a function of transmit power, Figure 5.4. While for the PedA simulations, the average SNR is the same on all the receive antennas, the measured receive SNR differs from one antenna to the other, with around 5 dB difference between the weakest and the strongest channel. Therefore, the optimum CQI and the measured curve differ even in the low SNR regime, since the feedback function Equation (4.1) expects a scalar SNR value that it assumes to be the SNR on all the antennas.

System Bandwidth	1.4 MHz, scheduled for a single UE
MIMO transmission mode	9
Carrier frequency	2.5 GHz ($\lambda = 12$ cm)
Transmit antennas	Kathrein 80010543-XX pol [6]
MIMO setup	4×4 double cross polarized
Number of XYΦ-table positions	100
Average feedback delay	467 ms

Table 5.1: Measurement parameters

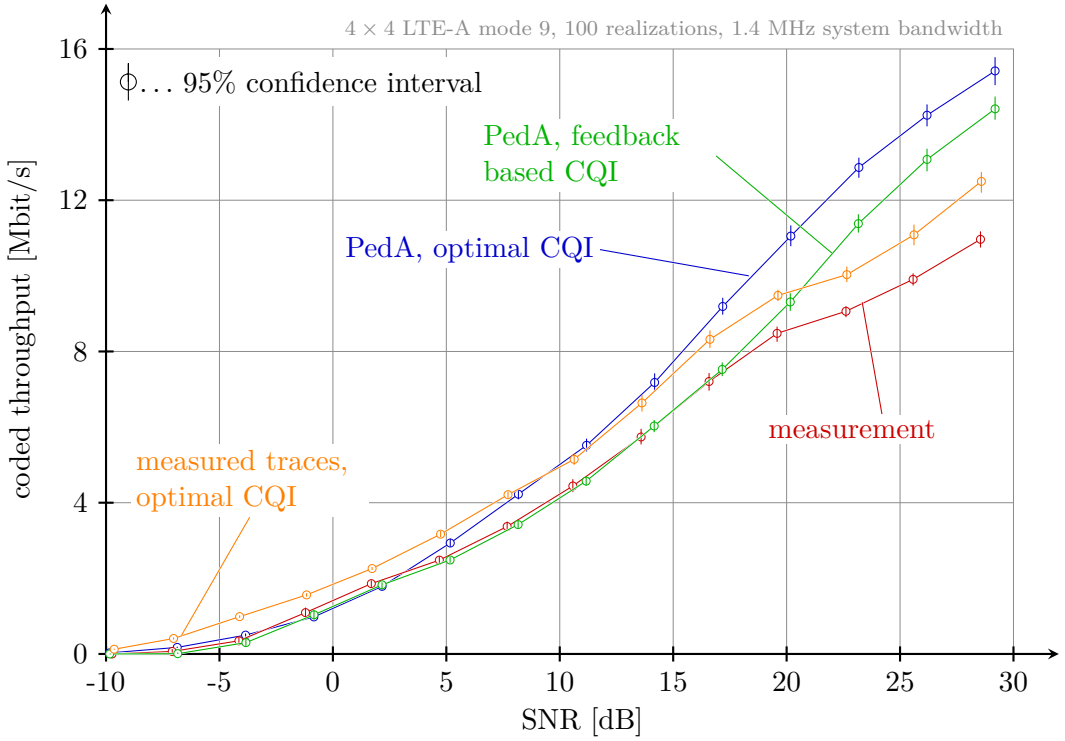

Figure 5.3: Comparison between simulated and measured throughput for both optimal and feedbackbased selection of MCS

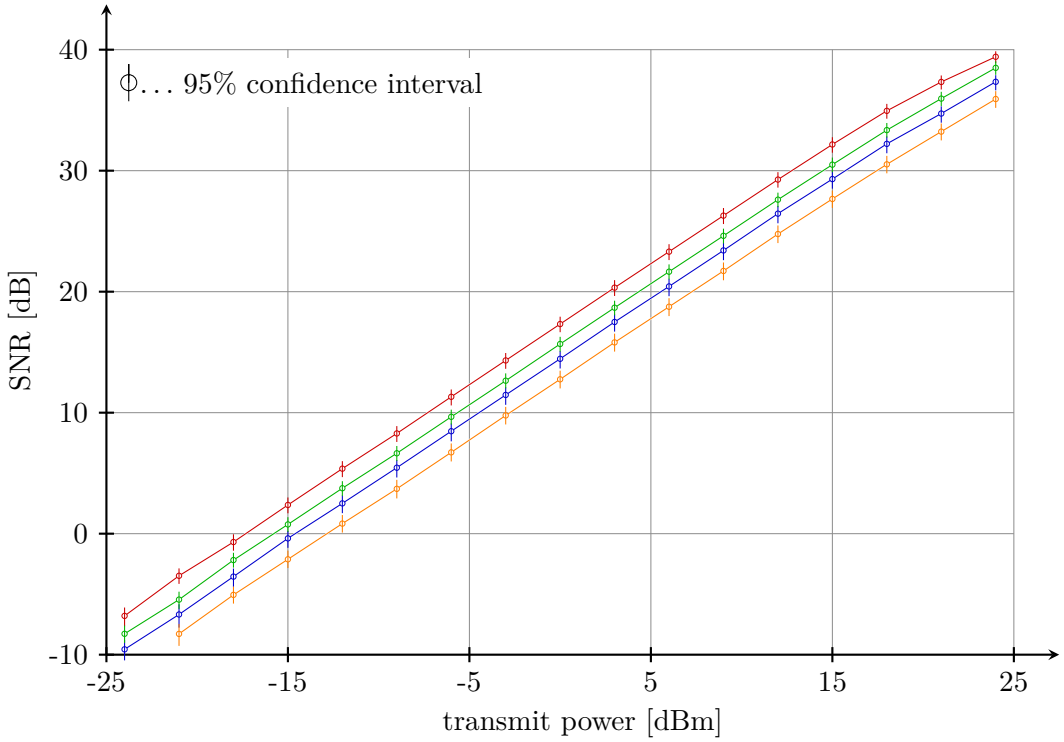

Figure 5.4: Measured average SNR for the four receive antennas plotted over transmit power

Chapter 6

Conclusion and Outlook

Throughout this work, a MATLAB software —responsible for signal generation and evaluation— has been implemented to allow for measurements incorporating real-time channel feedback with the Vienna MIMO Tested. The implementation spans the whole spectrum of physical layer signal processing in LTE, including channel coding, frequency selective scheduling, linear spatial precoding, channel estimation, equalization and many others.

The feedback based approach overcomes the limitations of the brute force method that has been used previously: It is now possible to measure MIMO schemes based on non codebook based precoding as well as higher order MIMO modes such as 4×4 LTE CLSM and 4×4 LTE-A mode 9, whose variety of possible parameter combinations exceed the practical limits of computational complexity for the brute force method.

In addition to the measurement software, a simulation environment has been created that allows for comparisons of measurements, measurement based simulations and purely simulative results. Consequently, the impairments of a feedback based approach —that being the feedback delay and the imperfection of the feedback function— can be assessed and evaluated, enabling the distinction between those effects and others.

More over, a proof-of-concept measurement of 4×4 LTE-A transmission mode 9 has been conducted, demonstrating the feasibility of the feedback based approach as well as providing novel measurement based performance figures for LTE-A downlink transmission.

Due to the comprehensive implementation, many aspects of LTE can now be evaluated by real world measurements, including the impact of HARQ, the effect of frequency selective modulation and coding, the performance of feedback strategies under real world conditions and others.

Whereas the current configuration of the Vienna MIMO Testbed only allows for a maximum of 4×4, LTE-A is specified to support up to 8×8 MIMO. The presented software can in principle also deal with an 8×8 setup, but the underlying hardware and daemon software are not ready for such a setup. However, a workaround combining two transmitters with 4 antennas each and a RF switch at the receiver for fast switching

between the two available sets of 4 receive antennas could be realized without purchasing additional hardware and rewriting the daemon software. Using this hardware setup in combination with the presented software, the measurement procedure for a "pseudo" 8×8 setup could be as follows:

1. Transmit pilot frame #1 simultaneously from two transmitters, switch the receive antenna set and transmit it again.
2. Combine the two four channel receive files to one 8 channel receive file, generate an 8 channel data frame, split it into two 4 channel files and load them back to the transmitters
3. Repeat the transmission and switching from step 1 with the data frame

To see if such an approach would be feasible, the signal processing delay constituting the main part of the delay could be assessed with `Simulate.m` without further ado. Subsequently, channel measurements can be conducted to see whether the constancy of the channel is long enough to justify this approach.

Bibliography

[1] 3GPP. *Technical Specification Group Radio Access Network; (E-UTRA) and (E-UTRAN); Base Station radio transmission and reception ; (Release 10)*. Tech. rep. 07/2013. URL: http://www.3gpp.org/ftp/Specs/html-info/36104.htm.

[2] 3GPP. *Technical Specification Group Radio Access Network; (E-UTRA) and (E-UTRAN); Physical Channels and Modulation; (Release 8)*. Tech. rep. 01/2010. URL: http://www.3gpp.org/ftp/Specs/html-info/36211.htm.

[3] 3GPP. *Technical Specification Group Radio Access Network; (E-UTRA) and (E-UTRAN); Physical Channels and Modulation; (Release 10)*. Tech. rep. 04/2013. URL: http://www.3gpp.org/ftp/Specs/html-info/36211.htm.

[4] 3GPP. *Technical Specification Group Radio Access Network; (E-UTRA) and (E-UTRAN); Physical layer procedures; (Release 10)*. Tech. rep. 07/2013. URL: http://www.3gpp.org/ftp/Specs/html-info/36213.htm.

[5] 3GPP. *Technical Specification Group Radio Access Network; (E-UTRA) and (E-UTRAN); Physical layer procedures; (Release 11)*. Tech. rep. 07/2013. URL: http://www.3gpp.org/ftp/Specs/html-info/36213.htm.

[6] *800 10543* 60° *XX-pol Panel Antenna 2300–2690 MHz*. Kathrein Inc., Scala Division. URL: http://antennasystems.com/Merchant2/pdf/800_10543.pdf (visited on 10/16/2013).

[7] *80010677 Dual Band Indoor Directional Antenna*. Kathrein Inc., Scala Division. URL: http://www.kathrein-scala.com/catalog/80010677.pdf (visited on 10/16/2013).

[8] 4G Americas. *3GPP Release 11: Understanding the Standards for HSPA+ and LTE-Advanced Enhancements*. 07/2013. URL: http://www.4gamericas.org/documents/3GPP%20Release%2011-%20ES_Final%20.pdf (visited on 10/05/2013).

[9] M Bossert, A Huebner, F Schuehlein, H Haas, and E Costa. "On cyclic delay diversity in OFDM based transmission schemes". In: *OFDM workshop*. Vol. 2. 2002.

[10] Sebastian Caban. "Testbed-based Evaluation of Mobile Communication Systems". PhD thesis. Institut für Nachrichtentechnik und Hochfrequenztechnik, 2009. URL: http://publik.tuwien.ac.at/files/PubDat_181156.pdf.

[11] G. Caire, G. Taricco, and E. Biglieri. "Capacity of bit-interleaved channels". In: *Electronics Letters* 32.12 (1996), pp. 1060–1061. ISSN: 0013-5194. DOI: 10.1049/el:19960754.

[12] Erik Dahlman, Stefan Parkvall, and Johan Sköld. *4G LTE/LTE-Andvanced for Mobile Broadband*. Elsevier Science, 2011. ISBN: 9780123854896.

[13] Armin Disslbacher-Fink. "Hardware-based Timing Synchronization". MA thesis. Institute of Telecommunications, Vienna University of Technology, 2011. URL: http://publik.tuwien.ac.at/files/PubDat_195758.pdf.

[14] J. Duplicy, B. Badic, R. Balray, R. Ghaffar, P. Horáth, F. Kaltenberger, R. Knopp, I. Z. Kovács, H. T. Nguyen, D. Tandur, and G. Vivier. "MU-MIMO in LTE Systems". In: *EURASIP Journal on Wireless Communications and Networking* (2011).

[15] Leonhard Edlinger. "Vienna Wireless Testbed". MA thesis. Institute of Telecommunications, Vienna University of Technology, 2012.

[16] Heinz Haderer. "Wireless Testbed Receiver". MA thesis. Institute of Telecommunications, Vienna University of Technology, 2012.

[17] Edin Huremovic. "Wireless Testbed Transmitter". MA thesis. Institute of Telecommunications, Vienna University of Technology, 2012.

[18] J. Colom Ikuno. "System Level Modeling and Optimization of the LTE Downlink". PhD thesis. Institute of Telecommunications, Vienna University of Technology, 2013.

[19] ITU. *Report ITU-R M.2134: Requirements related to technical performance for IMT-Advanced radio interface(s)*. Tech. rep. 2008.

[20] ITU. *Recommendation ITU-R M.1225: Guidelines for Evaluation of Radio Transmission Technologies for IMT-2000*. Tech. rep. 1997.

[21] Chaiman Lim, Taesang Yoo, B. Clerckx, Byungju Lee, and Byonghyo Shim. "Recent trend of multiuser MIMO in LTE-advanced". In: *Communications Magazine, IEEE* 51.3 (2013), pp. 127–135. ISSN: 0163-6804. DOI: 10.1109/MCOM.2013.6476877.

[22] *LTE Advanced Link Level Simulator*. URL: http://www.nt.tuwien.ac.at/research/mobile-communications/lte-simulators/ (visited on 10/17/2013).

[23] M. Lerch and M. Rupp. "Measurement-Based Evaluation of the LTE MIMO Downlink at Different Antenna Configurations". In: *Proc. of 17th International ITG Workshop on Smart Antennas (WSA 2013)*. Stuttgart, Germany, 03/2013.

[24] M. Meidlinger and Q. Wang. "Performance Evaluation of LTE Advanced Downlink Channel Estimators". In: *19th International Conference on Systems, Signals and Image Processing (IWSSIP)*. Wien: Proc. IWSSIP 2012, 04/2012, pp. 252–255.

[25] M. Simko, Q. Wang, and M. Rupp. "Optimal pilot symbol power allocation under time-variant channels". In: *EURASIP Journal on Wireless Communications and Networking* 225 (2012).

[26] Christian Mehlführer, Martin Wrulich, Josep Colom Ikuno, Dagmar Bosanska, and Markus Rupp. "Simulating the Long Term Evolution Physical Layer". In: *Proc. of the 17th European Signal Processing Conference (EUSIPCO 2009)*. Glasgow, Scotland, 08/2009. URL: http://publik.tuwien.ac.at/files/PubDat_175708.pdf.

[27] Martin Klaus Mueller. "Feedback-based LTE-Downlink Measurements". MA thesis. Institute of Telecommunications, Vienna University of Technology, 2013.

[28] J.C. Mundarath and J.H. Kotecha. "Multi-User Multi-Input Multi-Output (MU-MIMO) Downlink Beamforming Systems with Limited Feedback". In: *Global Telecommunications Conference, 2008. IEEE GLOBECOM 2008. IEEE*. 2008, pp. 1–6. DOI: 10.1109/GLOCOM.2008.ECP.737.

[29] Young-Han Nam, Y. Akimoto, Younsun Kim, Moon-il Lee, K. Bhattad, and A. Ekpenyong. "Evolution of reference signals for LTE-advanced systems". In: *Communications Magazine, IEEE* 50.2 (2012), pp. 132–138. ISSN: 0163-6804. DOI: 10.1109/MCOM.2012.6146492.

[30] S. Schwarz, C. Mehlführer, and M. Rupp. "Calculation of the Spatial Preprocessing and Link Adaption Feedback for 3GPP UMTS/LTE". In: *IEEE Proceedings of Wireless Advanced 2010*. London, 06/2010.

[31] S. Schwarz and M. Rupp. "Adaptive Channel Direction Quantization - Enabling Multi User MIMO Gains in Practice". In: *IEEE International Conference on Communications (ICC) 2012*. Ottawa, Canada, 06/2012, pp. 6947–6952.

[32] S. Shim, Jin Sam Kwak, R.W. Heath, and J.G. Andrews. "Block diagonalization for multi-user MIMO with other-cell interference". In: *Wireless Communications, IEEE Transactions on* 7.7 (2008), pp. 2671–2681. ISSN: 1536-1276. DOI: 10.1109/TWC.2008.070093.

[33] *The Seven Modes of MIMO in LTE*. Tech. rep. Telesystem Innovations, 2009. URL: http://www.tsiwireless.com/docs/whitepapers/The%20Seven%20Modes%20of%20MIMO%20in%20LTE.PDF (visited on 11/05/2013).

Appendix A

Acronymes

ASIC Application specific integrated circuit

AWGN Additive White Gaussian Noise

BICM Bit Interleaved Coded Modulation

CoMP Coordinated MultiPoint

CP Cyclic Prefix

CQI Channel Quality Indicator

CSI Channel State Information

CSI-RS CSI Reference Symbols

CDD Cyclic Delay Diversity

CLSM Closed Loop spatial Multiplexing

CVQ Channel Vector Quantization

C-RS Cell specific Reference Symbols

DFT Discrete Fourier Transform

DVB-T Digital Video Broadcast - Terrestrial

eNodeB Generalization of a base station in LTE-(A) terminology

FDD Frequency Division Duplexing

FFT Fast Fourier Transform

HARQ Hybrid Automatic Repeat reQuest

HSDPA High Speed Downlink Packet Access

IDFT Inverse Discrete Fourier Transform

IF Intermediate Frequency

IFFT Inverse Fast Fourier Transform

LAN Local Area Network

LNA Low Noise Amplifier

LTE Long Term Evolution

LTE-A LTE-Advanced

MAC Medium Access Control

MCS Modulation and Coding Scheme

MI Mutual Information

MIMO Multiple Input- Multiple Output

MU-MIMO Multi User MIMO

MSE Channel Estimation Mean Squared Error

OFDM Orthogonal Frequency-Division Multiplexing

OLSM Open loop spatial multiplexing

PHY Abbreviation for physical layer

PMI Precoding Matrix Indicator

QAM Quadrature Amplitude Modulation

RAID Redundant Array of Independent Disks

RB Resource Block

RE Resource Element

RF Radio Frequency

RI Rank Indicator

RS Reference Symbol

SIMO Single Input - Multiple Output

SISO Single Input - Single Output

SNR Signal to Noise Ratio

SINR Signal to Interference plus Noise Ratio

SU-MIMO Single User MIMO

TD Transmit Diversity

TTI Time-Transmission Interval

UE User Equipment

UE-RS User specific Reference Symbols

WiMAX Worldwide Interoperability for Microwave Access

ZF Zero Forcing